

## Nucleon structure functions from measurements of inelastic neutrino and antineutrino interactions

S. M. Heagy,\* A. Benvenuti,<sup>†</sup> D. Cline, D. D. Reeder, T. Trinko, and D. R. Winn<sup>‡</sup>

*Department of Physics, University of Wisconsin, Madison, Wisconsin 53706*

F. Bobisut,<sup>§</sup> P. S. Cooper,<sup>||</sup> M. G. D. Gilchriese,<sup>¶</sup> and A. K. Mann

*Department of Physics, University of Pennsylvania, Philadelphia, Pennsylvania 19104*

M. E. Johnson, R. Lundy, R. Mori,\*\* and R. Stefanski

*Fermi National Accelerator Laboratory, Batavia, Illinois 60510*

P. McIntyre and J. A. Rich<sup>††</sup>

*Department of Physics, Harvard University, Cambridge, Massachusetts 02138*

T. Y. Ling

*Department of Physics, Ohio State University, Columbus, Ohio 43210*

R. Imlay<sup>††</sup>

*Department of Physics, Rutgers University, New Brunswick, New Jersey 08903*

(Received 3 September 1980)

This paper presents the final results on charged-current neutrino and antineutrino interactions with nuclei from experiment E-310 at Fermi National Accelerator Laboratory. The data sample, consisting of 21 578 neutrino-induced and 7358 antineutrino-induced events within the fiducial region in the energy range  $20 < E < 325$  GeV, is exhibited first to demonstrate the basic properties and kinematic regions represented. The dependence of the nucleon structure functions on the dimensionless variable  $x$  and on neutrino energy is then described. Lastly, the variations of the structure functions with  $x$  and  $Q^2$  are presented. The emphasis throughout has been to understand the effects on the final results of uncertainties in the systematic corrections required by the data. Comparisons with the results of other neutrino experiments are made.

### I. INTRODUCTION

Serious study of the lepton-nucleon interaction and of nucleon structure became feasible with the advent of lepton scattering experiments at high energy. The earliest experiments motivated the development of the quark-parton model (QPM)<sup>1</sup> which, as is well known, describes remarkably well the features of nucleon properties and of lepton-nucleon interactions, as well as certain other processes. Deviations from the QPM have, however, been observed in scattering experiments with neutral and charged leptons. In particular, (Bjorken) scale invariance,<sup>2</sup> which was assumed in the QPM, was found to be broken through the production of charmed quarks and through an intrinsic dependence of the nucleon structure functions themselves on a dimensional variable,  $Q^2$ , the square of the momentum transferred to the parton in the scattering process.

On average the scale-breaking effects are not large (~10%), although in certain regions of the relevant dynamical variables they are more significant. Quantum chromodynamics<sup>3</sup> (QCD) is a field theory that takes into account interactions among partons and attempts thereby to provide a

detailed quantitative explanation of the scaling violations. In leading order in QCD the principal results of the QPM remain unchanged, except that the nucleon structure functions (parton distributions) become weak (logarithmic) functions of  $Q^2$  as well as of the dimensionless variable  $x$  that specifies the fraction of the nucleon momentum carried by the parton in the lepton-parton collision.

It is a consequence of this relatively weak dependence of the structure functions on  $Q^2$  that one of the main tasks of lepton-nucleon scattering experiments at present is to obtain large data samples subject to only small systematic uncertainties with which to confront the theory. It is particularly important to obtain results from experiments that differ significantly in experimental method, and to make detailed intercomparisons of such results to arrive at an internally consistent world data sample to compare with refined theoretical predictions.

In this paper we present the final results extracted from a series of measurements of charged-current neutrino ( $\nu$ ) and antineutrino ( $\bar{\nu}$ ) interactions with nuclei carried out at Fermilab. Brief descriptions of the experiment and of cer-

tain preliminary results on nucleon structure functions<sup>4</sup> and multimuo final states<sup>5</sup> were given previously. Here emphasis is placed on understanding the effects of uncertainties in required systematic corrections on the results derived from a statistically significant data sample, and on comparison of these results with those of other experiments.

Section II of this paper discusses briefly the theoretical framework that underlies the experiment and the method of data analysis. In Sec. III the apparatus and techniques of data acquisition are described. Section IV presents results and comparisons with other experiments. Section V is devoted to a summary and conclusions.

## II. THEORETICAL FRAMEWORK

The development of the theory of lepton-nucleon inelastic scattering has been summarized in several excellent reviews.<sup>3</sup> The following is a brief summary of the definitions and equations required to interpret experimental data in the context of the QPM, and to extend that interpretation to the leading-order result of QCD, i.e., the  $Q^2$  dependence of the structure functions.

### A. Bjorken scaling

The basic quantities necessary to describe quantitatively deep-inelastic lepton-nucleon scattering processes (in which  $E_{\text{lepton}} \gg M_{\text{nucleon}} \gg m_{\text{lepton}}$ ) are three nucleon structure functions  $W_1$ ,  $W_2$ , and  $W_3$ , which in general are functions of two dynamical variables defined by

$$\nu = p \cdot q / M = E_H + M \approx E_H \quad (2.1)$$

and

$$Q^2 = -q^2 = (k - k')^2 = 4E_\nu E_\mu \sin^2 \frac{\theta_{\mu\nu}}{2}, \quad (2.2)$$

where  $p$  is the initial-nucleon four-momentum,  $k$  and  $k'$  the initial- and final-state lepton four-momenta, and  $M$  is the nucleon mass. Equations (2.1) and (2.2) also express  $\nu$  and  $Q^2$  in terms of directly measured quantities:  $E_H$ , the hadronic energy produced in the collision, and  $p_\mu$  and  $\theta_{\mu\nu}$ , the outgoing muon momentum and angle, respectively. The incident neutrino energy is then  $E_\nu = E_H + E_\mu$ .

It was pointed out by Bjorken that for collisions in which both  $\nu$  and  $Q^2$  were much larger than the masses of any real particle participating in the collision, the dimensionless structure functions  $W_1$ ,  $\nu W_2$ , and  $\nu W_3$  would depend only on the quantity

$$x = Q^2 / 2M\nu \quad (2.3)$$

and Bjorken scaling would prevail. Under this condition one defines three scale-invariant structure functions

$$\begin{aligned} 2MW_1(\nu, Q^2) &\rightarrow F_1(x), \\ \nu W_2(\nu, Q^2) &\rightarrow F_2(x), \\ \nu W_3(\nu, Q^2) &\rightarrow F_3(x), \end{aligned} \quad (2.4)$$

and the differential cross sections for charged-current neutrino- and antineutrino-nucleon inelastic scattering are

$$\begin{aligned} \frac{d^2\sigma^{\nu, \bar{\nu}}}{dx dy} &= \frac{G^2 ME}{\pi} \left[ (1-y) F_2^{\nu, \bar{\nu}}(x) + y^2 x F_1^{\nu, \bar{\nu}}(x) \right. \\ &\quad \left. \mp \left( y - \frac{y^2}{2} \right) x F_3^{\nu, \bar{\nu}}(x) \right], \end{aligned} \quad (2.5)$$

where we follow the sign convention in our earlier papers<sup>4,5</sup> and take  $x F_3(x)$  as intrinsically negative so that the upper sign is for neutrinos and the lower sign for antineutrinos,  $G$  is the Fermi weak-coupling constant,  $E$  is the incident neutrino (antineutrino) energy in the laboratory frame, and

$$y = \frac{\nu}{E} \approx \frac{E_H}{E} \quad (2.6)$$

measures the inelasticity of the interaction. It is useful to define the ratios

$$B = - \frac{\int x F_3(x) dx}{\int F_2(x) dx} \quad (2.7)$$

and

$$\begin{aligned} R &= \left( \frac{\int F_2(x) dx}{\int 2x F_1(x) dx} \right) - 1 \\ &= \frac{\int 2F_S(x) dx}{\int [F_L(x) + F_R(x)] dx} = \frac{\sigma_S}{\sigma_T}, \end{aligned} \quad (2.8)$$

where  $F_L$ ,  $F_R$ , and  $F_S$  represent structure functions for left-handed, right-handed, and scalar currents and are related to  $F_1$ ,  $F_2$ , and  $F_3$  by

$$\begin{aligned} F_L(x) &= 2x F_1(x) - x F_3(x), \\ F_R(x) &= 2x F_1(x) + x F_3(x), \\ F_S(x) &= F_2(x) - 2x F_1(x), \end{aligned} \quad (2.9)$$

and  $\sigma_S/\sigma_T$  is the ratio of scalar to transverse virtual-boson absorption cross sections, and we have neglected a term of order  $4M^2 x^2 / Q^2$  in Eq. (2.8). The differential cross sections of Eq. (2.5) integrated over  $x$  can then be written

$$\begin{aligned} \frac{d\sigma^{\nu, \bar{\nu}}}{dy} &= \frac{G^2 ME}{\pi} \int F_2^{\nu, \bar{\nu}}(x) dx \left[ 1 - (1 \mp B^{\nu, \bar{\nu}}) \left( y - \frac{y^2}{2} \right) \right. \\ &\quad \left. - f(R^{\nu, \bar{\nu}}) \frac{y^2}{2} \right] \end{aligned} \quad (2.10)$$

with  $f(R^{\nu, \bar{\nu}}) = R^{\nu, \bar{\nu}} / (R^{\nu, \bar{\nu}} + 1)$  and the upper sign

refers to neutrinos and the lower sign to antineutrinos. Equation (2.10) is convenient for studying the behavior of  $B$  and  $R$  by means of measured event distributions in  $x$  and  $y$ .

### B. Quark-parton model

In the four-quark model ( $u, d, s, c$ ) with spin- $\frac{1}{2}$  quarks the structure functions  $F_2(x)$  and  $x F_3(x)$  for *isoscalar* targets can be expressed in terms of quark distributions defined on the *proton*. These are given by

$$F_2^\nu(x) = F_2^{\bar{\nu}} = x [u(x) + d(x) + s(x) + c(x) + \bar{u}(x) + \bar{d}(x) + \bar{s}(x) + \bar{c}(x)], \quad (2.11)$$

$$x F_3^\nu(x) = -x [u(x) + d(x) + s(x) - c(x) - \bar{u}(x) - \bar{d}(x) + \bar{s}(x) - \bar{c}(x)], \quad (2.12)$$

$$x F_3^{\bar{\nu}}(x) = -x [u(x) + d(x) + c(x) - s(x) - \bar{u}(x) - \bar{d}(x) + \bar{c}(x) - \bar{s}(x)], \quad (2.13)$$

and by assumption

$$\begin{aligned} \frac{3}{4} \frac{\pi}{G^2 ME} \left( \frac{d\sigma^\nu}{dx} + \frac{d\sigma^{\bar{\nu}}}{dx} \right) &= \frac{3}{4} F_2(x) + \frac{1}{2} x F_1(x) - \frac{1}{4} [x F_3^\nu(x) - x F_3^{\bar{\nu}}(x)] \\ &= x [u(x) + d(x) + \frac{3}{2} s(x) + \frac{1}{2} c(x) + \bar{u}(x) + \bar{d}(x) + \frac{3}{2} \bar{s}(x) + \frac{1}{2} \bar{c}(x)] \end{aligned} \quad (2.17)$$

and

$$\begin{aligned} \frac{3}{2} \frac{\pi}{G^2 ME} \left( \frac{d\sigma^\nu}{dx} - \frac{d\sigma^{\bar{\nu}}}{dx} \right) &= -\frac{1}{2} [x F_3^\nu(x) + x F_3^{\bar{\nu}}(x)] \\ &= x [u(x) + d(x) - \bar{u}(x) - \bar{d}(x)]. \end{aligned} \quad (2.18)$$

In Eq. (2.17),  $\frac{3}{4} F_2(x) + \frac{1}{2} x F_1(x) = F_2(x)$ , provided the assumption  $2x F_1(x) = F_2(x)$  holds. Similarly, Eq. (2.10) yields

$$\frac{1}{2} \frac{\pi}{G^2 ME} \left( \frac{d\sigma^\nu}{dy} + \frac{d\sigma^{\bar{\nu}}}{dy} \right) = \int F_2(x) dx \left[ \left( 1 - y + \frac{y^2}{2} \right) + \frac{1}{2} (B^\nu - B^{\bar{\nu}}) \left( y - \frac{y^2}{2} \right) + f(R) \frac{y^2}{2} \right] \quad (2.19)$$

with

$$(B^\nu - B^{\bar{\nu}}) = \Delta B = \frac{4 \int x [\bar{s}(x) - \bar{c}(x)] dx}{\int F_2(x) dx} \quad (2.20)$$

and

$$f(R) = \frac{R}{R+1}. \quad (2.21)$$

Furthermore, subtracting Eq. (2.18) from Eq. (2.17), multiplying by  $\frac{1}{2}$ , and using  $x s(x) = x \bar{s}(x)$ , etc., gives the fractional momentum distribution of the antiquark combination

$$\frac{1}{8} \left( 9 \frac{d\sigma^{\bar{\nu}}}{dx} - 3 \frac{d\sigma^\nu}{dx} \right) = x [\bar{u}(x) + \bar{d}(x) + \frac{3}{2} \bar{s}(x) + \frac{1}{2} \bar{c}(x)]. \quad (2.22)$$

The corresponding distribution of a somewhat dif-

$$F_2(x) = 2x F_1(x). \quad (2.14)$$

Here, for example,  $u(x)$  measures the probability of finding a parton (in this case a  $u$  quark) in the proton with fractional momentum  $x$ .

The differential cross sections can then be written in terms of quark-momentum distributions in units of  $G^2 ME/\pi$ ,

$$\begin{aligned} \frac{d\sigma^\nu}{dx dy} &= x \{ [u(x) + d(x) + 2s(x)] \\ &\quad + (1-y)^2 [\bar{u}(x) + \bar{d}(x) + 2\bar{c}(x)] \} \end{aligned} \quad (2.15)$$

and

$$\begin{aligned} \frac{d\sigma^{\bar{\nu}}}{dx dy} &= x \{ [\bar{u}(x) + \bar{d}(x) + 2\bar{s}(x)] \\ &\quad + (1-y)^2 [u(x) + d(x) + 2c(x)] \}. \end{aligned} \quad (2.16)$$

Equations (2.5), (2.10), (2.15), and (2.16) provide the means with which to extract structure functions and quark momentum distributions from the data. Integration over  $y$  yields

ferent antiquark combination can be obtained from Eqs. (2.15) and (2.16) in the form

$$\frac{\pi}{G^2 ME} \left[ \frac{d\sigma^{\bar{\nu}}}{dx dy} - (1-y)^2 \frac{d\sigma^\nu}{dx dy} \right]_{y=1} = x [\bar{u}(x) + \bar{d}(x) + 2\bar{s}(x)] \quad (2.23)$$

which makes use only of antineutrino  $x$ -distribution data, apart from a small contribution from the second term on the left-hand side. Finally, one obtains from the shapes of antineutrino  $y$ -distributions essentially the same quantity

$$\frac{1}{2} (1 - B^{\bar{\nu}}) = \frac{\int x [\bar{u}(x) + \bar{d}(x) + 2\bar{s}(x)] dx}{\int F_2(x) dx} \quad (2.24)$$

which is just the antiquark fractional momentum in the proton (except for the small charm contribution).

### C. QCD: $Q^2$ dependence of the structure functions

The QPM with scale invariance includes no  $Q^2$  dependence of the structure functions since it is a theory of free quarks. QCD introduces quark-quark and quark-gluon interactions analogous to electron-electron and electron-photon interactions in quantum electrodynamics. The quark-gluon coupling constant  $\alpha_s$  decreases with  $Q^2$  such that for  $Q^2 \gg 1 \text{ GeV}^2$  perturbative calculations are considered justifiable. As  $Q^2$  increases further, the quark-quark and quark-gluon interactions become smaller, finally vanishing as  $Q^2 \rightarrow \infty$ , the condition of asymptotic freedom.

At high  $Q^2$  quarks can radiate gluons thus reducing the fraction of the nucleon momentum carried by the quarks. The fractional momentum carried by the sea quarks is expected to increase with increasing  $Q^2$ , but mostly at low  $x$ . Qualitatively, then, the structure functions  $F_2(x, Q^2)$  and  $x F_3(x, Q^2)$  should increase at small  $x$  as  $Q^2$  increases. Quark-gluon interactions also may give rise to transverse quark momenta which can induce a nonzero scalar cross section and thus violate the condition  $2xF_1(x) = F_2(x)$ .

### III. APPARATUS AND DATA ACQUISITION

This section presents the salient features of the apparatus and of the data-gathering technique. Apparatus components and performance are discussed to clarify certain features of the data and the corrections applied to the data. A more detailed description of the apparatus and the technique can be found in Ref. 6.

#### A. Neutrino beams

The experiment was situated on the N-0 beam line<sup>7</sup> (see Fig. 1) at Fermi National Accelerator Laboratory. Resonant extraction from the accelerator produced about  $10^{13}$  protons on a 12-in. beryllium oxide target with beam spills of duration 2–20 msec. Secondary pions and kaons were handled in either of two ways downstream of the target. The first method, shown in Fig. 2(a), employed a quadrupole triplet (QT) focusing arrange-

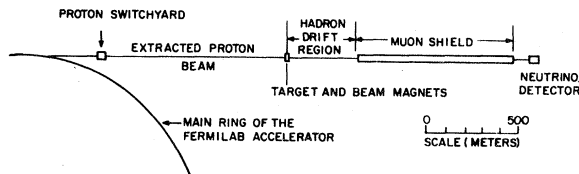


FIG. 1. Schematic diagram of the N-0 beam line used to produce the neutrino and antineutrino beams used in the experiment.

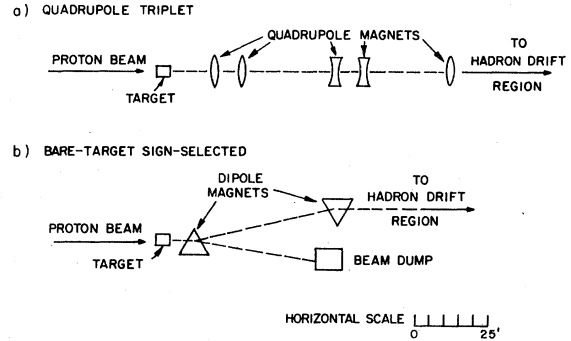


FIG. 2. (a) The quadrupole triplet (QT) post-proton-target arrangement. The quadrupole triplet produced simultaneously focused beams of charged hadrons of both signs resulting in a mixed neutrino and antineutrino beam. (b) Bare-target sign-selected (BTSS) post-proton-target arrangement. The BTSS produced hadron beams of selected charge resulting in a reasonably pure neutrino or antineutrino beam.

ment<sup>8</sup> designed to provide a point-to-parallel focus of particles of both charges with momentum 225 GeV. The QT system enhanced the higher-energy neutrino (antineutrino) component of the beam relative to the low-energy component. The average energy of neutrino- and antineutrino-induced events was 90 and 60 GeV, respectively. About 14% of the neutrino-induced events were above 200-GeV total energy. The ratio of raw events in the detector fiducial region from antineutrinos and from neutrinos in the QT beam was about 1:6.

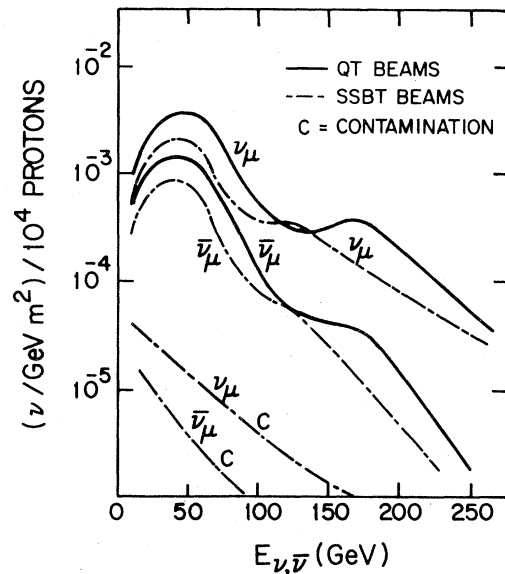


FIG. 3. Calculated neutrino and antineutrino fluxes as functions of energy for the various beam-line arrangements. The two curves labeled *c* represent the anti-particle contamination in the BTSS beams.

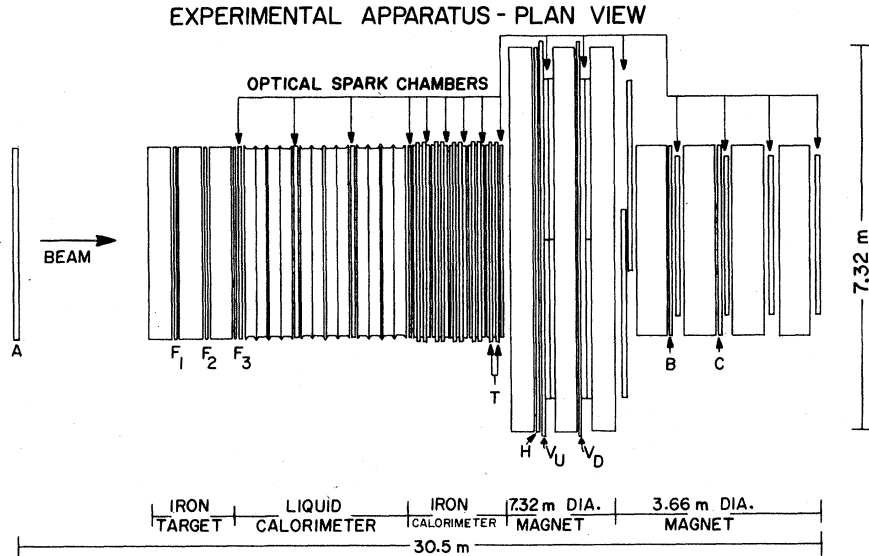


FIG. 4. Plan view of the experimental apparatus indicating the trigger counters, spark-chamber positions, calorimeters, and muon spectrometer as described in the text.

The other hadron-collecting method consisted of a dogleg of two dipole magnets in which particles of a given electric charge were directed along the beam line and the opposite charge component dumped.<sup>9</sup> This yielded sign-selected beams of hadrons with no focusing elements involved. These bare-target, sign-selected hadron beams (BTSS) give rise in turn to reasonably pure neutrino and

antineutrino beams. The BTSS arrangement is schematically illustrated in Fig. 2(b). The calculated fluxes for the two modes of focusing are shown in Fig. 3.

The selected secondary hadrons were allowed to decay in a 400-m drift space producing the neutrinos (antineutrinos) seen at the detector. Approximately 10% of the hadrons reaching the drift space decayed yielding about  $10^9$  neutrinos/sec incident on the detector. The muons associated with the decay were absorbed in a 1000-m earth shield. About five muons/spill penetrated the shield and hit the charged-particle anticounter in front of the detector.

Beam intensity was monitored by a secondary-emission monitor (SEM) and by a toroidal current transformer. The SEM and toroid agreed to within 5%. Beam-position monitors checked the proton-beam position relative to the target. In addition, a scintillation counter orthogonal to the target monitored secondary hadron production to ensure proper targeting. A total of  $8 \times 10^{18}$  protons struck the target during the course of the experiment.

#### B. Apparatus overview

The experimental apparatus consisted of two major parts: the interaction targets and calorimeters and a large acceptance muon spectrometer. The calorimeters measured the hadronic energy deposited in a neutrino interaction while the spectrometer determined the outgoing muon momentum vector.

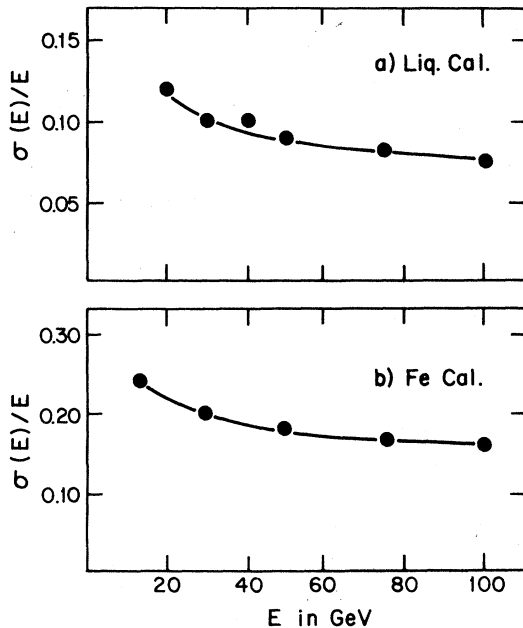


FIG. 5. Resolution curves for the liquid and the iron-plate (Fe) calorimeters. Note that the liquid calorimeter has about a factor-of-2 better resolution than the iron-plate calorimeter.

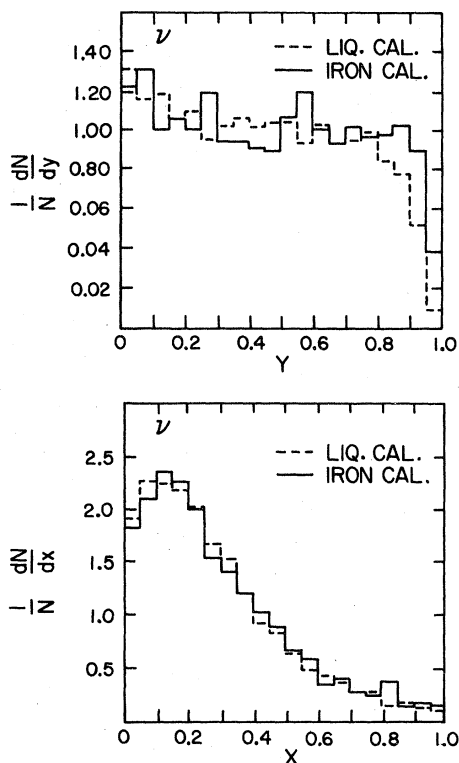


FIG. 6. Comparison of Bjorken  $x$  and  $y$  distributions from the liquid and iron-plate calorimeters. The distributions have been corrected for acceptance and radiative effects. The  $y$  distributions are restricted to  $x < 0.8$  to remove quasielastic events.

At the upstream end of the apparatus shown in Fig. 4 was the anticounter  $A$ . Downstream was an iron target of mass 250 metric tons from which only multimMuon events were studied and which contained the three counters  $F_1$ ,  $F_2$ , and  $F_3$ . No calorimetry was performed in the iron target, and events from this target were not utilized in the single-muon analysis.

Following the iron target was a pure-liquid-scintillator calorimeter<sup>6(a)</sup> composed of three sections, each subdivided into four optically separated segments. A wide-gap optical spark chamber was placed between each section. The target mass inside the fiducial volume ( $2.4 \text{ m} \times 2.4 \text{ m} \times 5.5 \text{ m}$ ) was 30 metric tons. The liquid calorimeter provided excellent energy resolution, as shown in Fig. 5(a), and good response to hadron energy depositions as low as 1 GeV.

Downstream of the liquid calorimeter was an iron-plate calorimeter composed of five modules each of which included a wide-gap spark chamber, two 10-cm-thick iron plates, and two 10-cm-thick liquid-scintillator counters. The total mass in the fiducial volume ( $3.1 \text{ m} \times 3.1 \text{ m} \times 1.8 \text{ m}$ ) was 56 met-

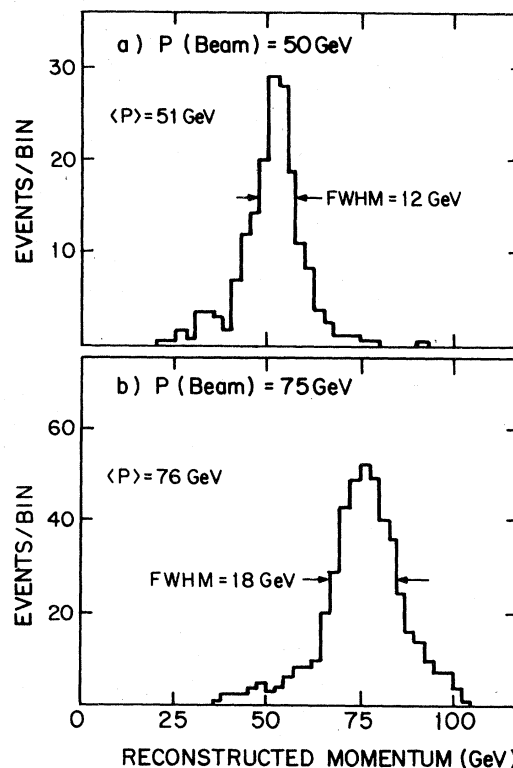


FIG. 7. Results of the spectrometer calibration for 50- and 75-GeV incident muons.

ric tons. The energy resolution of the iron calorimeter is shown in Fig. 5(b). The upstream part of the iron calorimeter provided a massive target close to the spectrometer while the downstream part served as a hadron filter between the interaction region and the spectrometer.

The muon spectrometer consisted of seven iron toroidal magnets, three 24 ft in diameter and four 12 ft in diameter. Interspersed between the magnet sections were optical wide-gap spark chambers for muon track detection. Various trigger counters ( $H$ ,  $V_u$ ,  $V_d$ ,  $B$ , and  $C$ ) were also present in the spectrometer, as shown in Fig. 4.

### C. Calorimetry

Each calorimeter was calibrated absolutely with hadrons of known energy. The hadron energy of a given event in either calorimeter could be expressed in units of the energy deposited by a minimum-ionizing particle in that calorimeter. To a good approximation, the relationship for each calorimeter was linear; for the liquid calorimeter the proportionality constant was 0.0959 GeV per equivalent minimum-ionizing particle, and the corresponding quantity for the iron calorimeter was 0.1812 GeV per equivalent minimum-ionizing

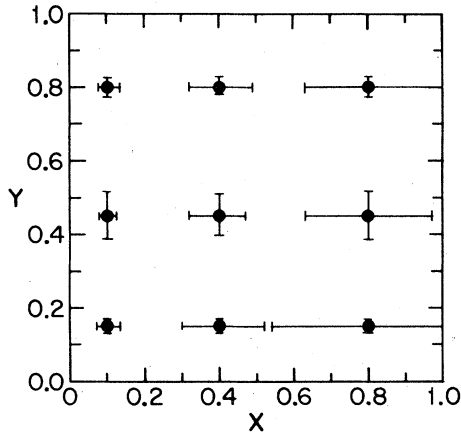


FIG. 8. Combined resolution in Bjorken  $x$  and  $y$  of the calorimeters and the muon spectrometer. The plot represents the resolution for the actual data sample in the energy range  $20 < E < 220$  GeV.

particle. The hadron energy determined by either calorimeter was independent of the location of the energy deposition within the calorimeter fiducial volume to within 10%. All calorimeter constants were continuously monitored by means of single minimum-ionizing particles and adjusted periodically to ensure uniform calorimeter response.

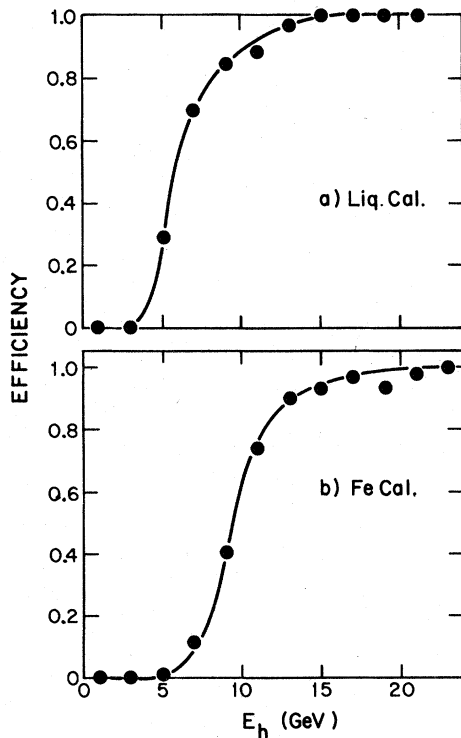


FIG. 9. Energy-trigger efficiencies (thresholds) for the liquid and iron-plate (Fe) calorimeters as functions of hadronic energy deposition,  $E_h$ . Note the difference in sensitivity of the two calorimeters.

The liquid and iron-plate calorimeters yielded independent information that was essentially identical, within measurement errors, as is illustrated by the distributions in the scaling variables  $x$  and  $y$  in Fig. 6.

#### D. Spectrometer and optics

The muon spectrometer measured the momentum vector of the final-state muon(s). The magnetic field in each of the seven sections of the spectrometer was toroidal in shape. The magnets were driven into saturation, and the variation in magnetic field was from 16 kG at the maximum radius to about 19 kG at the minimum radius. Muon trajectories were observed in optical wide-gap spark chambers and recorded photographically. Individual spark-chamber efficiencies were better than 95%. An advantage of the wide-gap spark chambers was that the tangent to the muon trajectory was determined in each chamber as well as the trajectory position. Tracks were recorded in two views with narrow-angle stereo ( $15^\circ$ ) and a third view at  $90^\circ$  to the axis of the stereo system.

Counter information was used to select events automatically for measurement, and the resulting frames were measured on the semiautomatic measuring machine (SAMM) of the film-analysis facility at Fermilab.<sup>10</sup> Events were reconstructed in space and a fit to muon momentum was made. The combined measurement, reconstruction, and fitting efficiency for events inside the fiducial region exceeded 95%. The optical system associated with the apparatus was periodically checked for distortions, which were removed in the spatial reconstruction of the sparks. A minimum of two sparks in the first four spark-chamber planes of the spectrometer were required for reliable momentum measurement. The angular acceptance of the apparatus with this requirement was about 400 mrad for events occurring furthest upstream and more than 600 mrad for events occurring furthest downstream.

The spectrometer, reconstruction, and fitting procedures were calibrated with incident muons of known momentum. The data for 50 and 75 GeV muons are shown in Fig. 7, and indicate a resolution  $\sigma(p)/p = 0.12$ . The resolution of the combined calorimeter system and the muon spectrometer as a function of the scaling variables  $x$  and  $y$  is shown in Fig. 8.

#### E. Triggering requirements

The detector was triggered, i.e., the spark chambers were pulsed, the calorimeter pulse heights read out, and the counters tagged, when

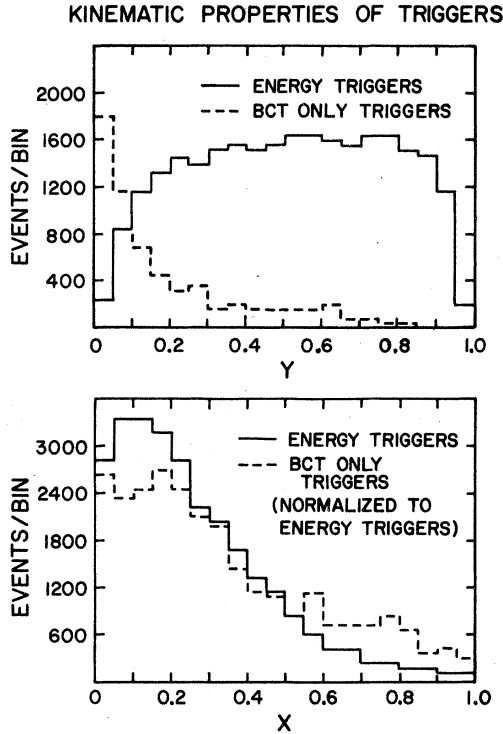


FIG. 10. Kinematic regions covered by pure muon (*BCT*) and by energy triggers (see text). The excess of events at large  $x$  in the *BCT* triggers is from the combined effects of resolution smearing and quasielastic events.

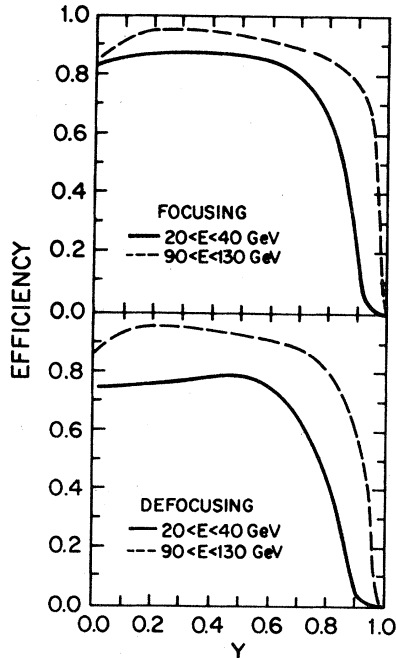


FIG. 11. Apparatus efficiency in two energy intervals with the spectrometer focusing and defocusing negative muons.

the properties of an event satisfied certain preset conditions. The requirements on triggers for single-muon events were of two kinds: those requiring only the presence of a muon [signified by a time coincidence of the  $T$ ,  $B$ , and  $C$  counters (see Fig. 4)], and those requiring a minimum deposition of energy in the calorimeters and a single hit in the  $H \cdot V$  hodoscope system. The efficiencies of the liquid and iron calorimeters as functions of the energy deposition  $E_H$  are shown in Fig. 9.

The relationship of the two kinds of triggers to the kinematics of events is illustrated in Fig. 10, which shows that the two triggers in combination accepted events over the entire range of the variable  $y$  (excepting only the region near  $y=1$  where the  $H \cdot V$  condition was not satisfied). The pure *BCT* triggers contain more events with  $x \geq 0.5$  than do the energy triggers due to the presence of quasielastic events ( $x=1$ ) and the limited resolution of the apparatus at large  $x$  (see Fig. 8).

The triggering scheme was actually designed to enhance the multimMuon signal relative to the single-muon interactions. This was accomplished either by using a later portion of the spill for single-muon triggers or by prescaling the single-muon triggers. The prescaling factors were experimentally determined by comparing triggers that simultaneously satisfied the nonprescaled multimMuon trigger requirements and also the prescaled single-muon trigger requirements. The prescaling factors were removed from the single-muon data to avoid possible distortions of the event distributions.

#### IV. DATA ANALYSIS AND RESULTS

This section presents the data accumulated in the experiment and various results extracted from the data. First, in subsections A–E the sample as a whole is described to demonstrate its basic properties and the kinematic regions represented. Next, in subsections F and G distributions in the dimensionless (Bjorken) variables  $x$  and  $y$  are discussed. Subsection H deals with the variation of  $\langle Q^2 \rangle / E$  with energy. Then, in subsections I and J the dependences of the nucleon structure functions on  $x$  and neutrino energy  $E_\nu$  are presented. Finally, subsection K deals with variations of the structure functions with  $x$  and  $Q^2$ .

##### A. Sample

The data sample consists of 21 578 neutrino and 7358 antineutrino events within the fiducial regions of the active calorimeter targets in the energy range  $20 < E < 325$  GeV. The distribution of events was 64% in the liquid calorimeter and 36% in the iron-plate calorimeter. Normally events would



be distributed in proportion to the fiducial masses of the calorimeters. However, the triggering utilized during part of the data acquisition excluded iron calorimeter events and produced the observed distribution. It is noteworthy that the hadron-energy resolution is about a factor of 2 better in the liquid calorimeter than in the iron calorimeter (Fig. 5).

#### B. Corrections

Corrections applied to the data fall into three major categories: acceptance, radiative, and resolution. The distribution of *corrected* events in the calorimeters corresponded to an average target composition that was isoscalar within 1% and required no correction.

The acceptance corrections dealt primarily with the geometrical efficiencies of the apparatus. Also included in the acceptance corrections were the triggering and data processing efficiencies. The acceptance corrections were calculated in a model-independent fashion by Monte Carlo methods and took into account the apparatus geometry, triggering configurations, calorimeter energy thresholds, incoming neutrino (antineutrino) spectra, beam dispersion, and reconstruction and fitting efficiencies for various event topologies. The corrections were recalculated each time any of the above factors was significantly altered. The acceptance

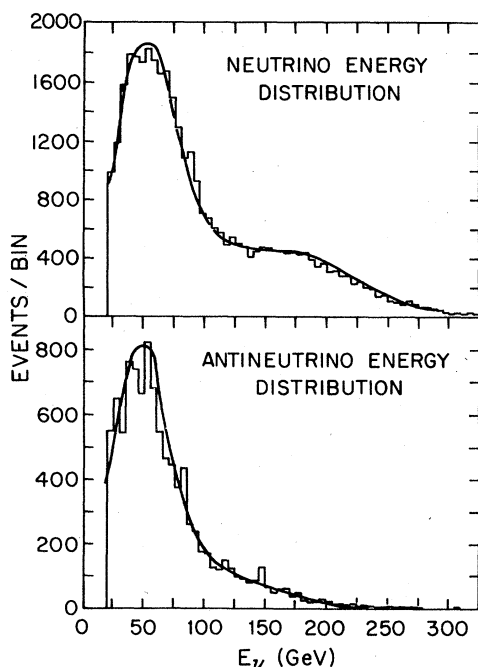


FIG. 12. Neutrino- and antineutrino-induced event energy spectra. The smooth curves are from the Monte Carlo simulation of the data used to study resolution and acceptance effects.

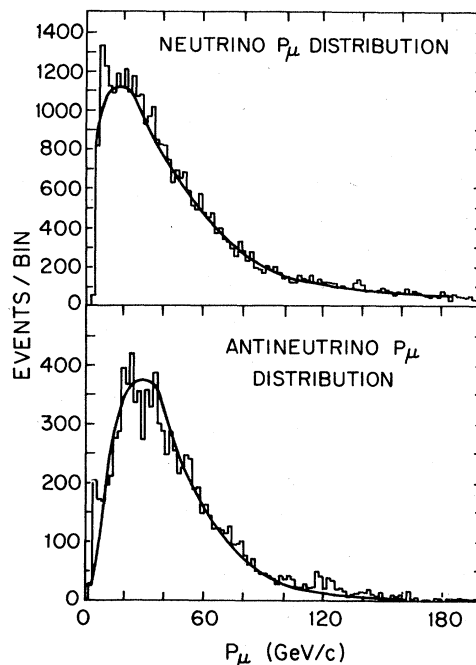


FIG. 13. Muon-momentum ( $p_\mu$ ) distributions for  $\nu$ - and  $\bar{\nu}$ -induced events. The smooth curves are from the Monte Carlo calculation.

corrections were calculated as functions of the scaling variables  $x$  and  $y$  and neutrino (antineutrino) energy, and applied event by event. The magnitude of the acceptance was large resulting in a correction of  $<15\%$  in all but the highest  $y$  region, where requirements on the number of chambers traversed in the spectrometer led to an effective muon momentum cutoff of  $\sim 4$  GeV. The corrections varied only slightly as a function of  $x$ . Examples of the acceptance are illustrated in Fig. 11.

The data have been corrected for radiative effects using calculations of De Rújula *et al.*<sup>11</sup> The radiative corrections which are of the order of 10% shift events from higher to lower  $y$ , and from lower to slightly higher values of  $x$ .

Resolution effects were studied by another Monte Carlo calculation, utilizing the general properties of the data sample and the apparatus resolution as measured in calibration runs. Figure 8, showing the resolution of the apparatus as a function of  $x$  and  $y$  averaged over all energies, was derived from the Monte Carlo calculation. In the  $x$  and  $y$  distributions presented in the following section resolution smearing was not removed from the distributions but was studied to determine the stability of the conclusions with respect to it. In determining the structure functions, however, the effects of smearing have been removed. The procedure entailed iteration until

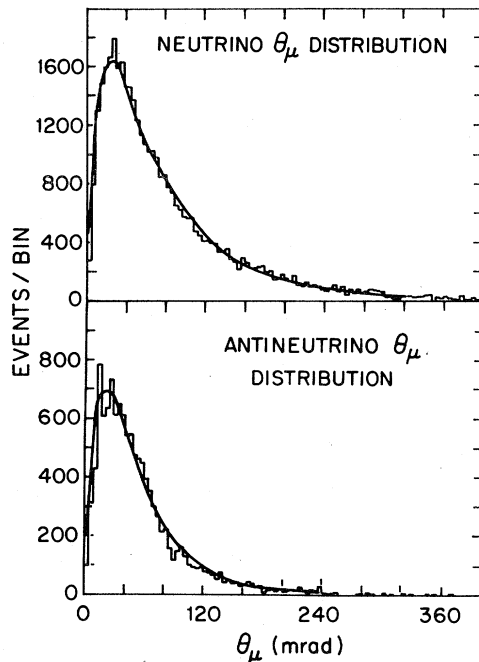


FIG. 14. Muon-angle ( $\theta_\mu$ ) distributions for  $\nu$ - and  $\bar{\nu}$ -induced events. The smooth curves are from the Monte Carlo calculations.

the Monte Carlo smeared distributions reproduced the data. The resolution corrections were less than 10% except at very small  $x$  ( $x < 0.1$ ) and very large  $x$  ( $x > 0.7$ ).

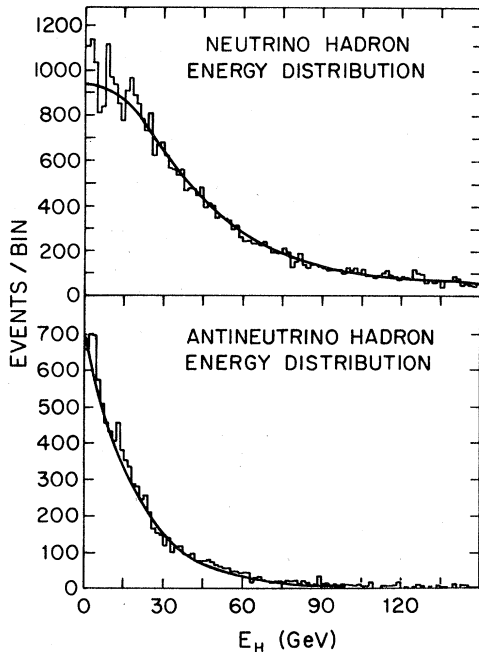


FIG. 15. Hadron-energy ( $E_H$ ) distributions for  $\nu$ - and  $\bar{\nu}$ -induced events. The smooth curves are from the Monte Carlo calculation.

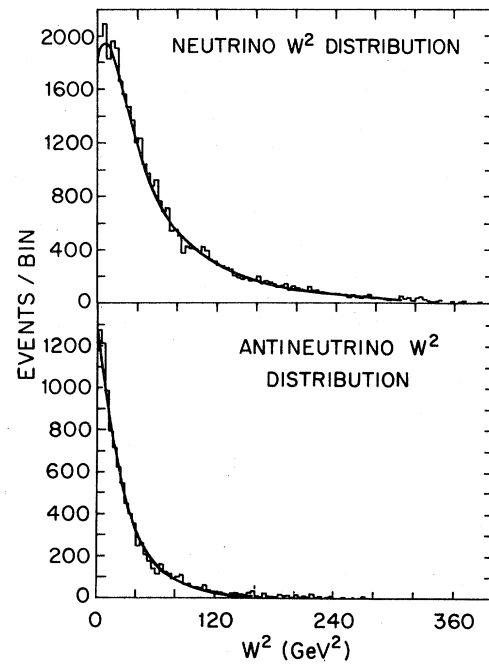


FIG. 16. Invariant-mass-squared ( $W^2 = M^2 + 2ME_H - Q^2$ ) distributions from  $\nu$ - and  $\bar{\nu}$ -induced events. The smooth curves are from the Monte Carlo calculation.

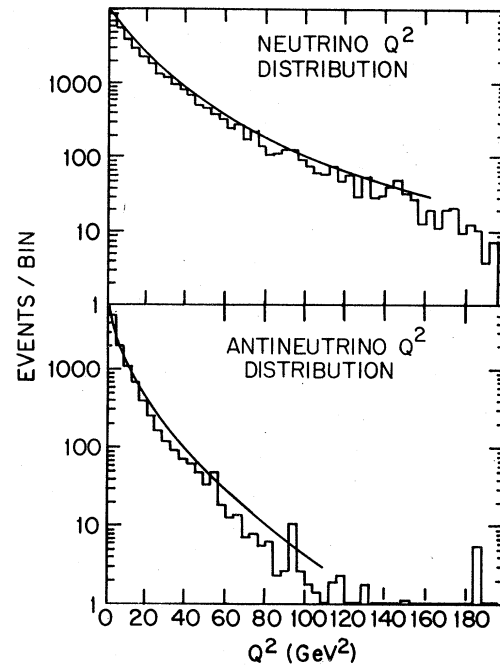


FIG. 17.  $Q^2$  distributions from  $\nu$ - and  $\bar{\nu}$ -induced events. The failure of the Monte Carlo calculation (smooth curve) to reproduce the data is due to the absence of  $Q^2$  dependence in the structure functions inserted in the Monte Carlo calculation. This discrepancy demonstrates directly the breakdown of scale invariance and the special significance of the variable  $Q^2$ .

## C. Basic properties of the sample

Figures 12–17 show, respectively, the measured distributions for neutrinos and antineutrinos in  $E_\nu, \bar{\nu}$ ,  $P_\mu$ ,  $\theta_\mu$ ,  $E_H$ ,  $W^2$ , and  $Q^2$  for the interval  $20 < E < 325$  GeV, all corrected for acceptance and radiative effects. Table I provides the average values of the parameters of those distributions.

In Fig. 12 the observed energy spectra of events reflect the mixture of the QT and BTSS spectra used in various portions of the data taking. The peaks below 100 GeV in both spectra represent events from  $\pi$ -decay neutrinos. In the spectrum for neutrino-induced events the shoulder visible above 100 GeV represents events primarily from neutrinos from  $K$  decay. The antineutrino spectrum does not exhibit as marked a neutrino component from  $K$  decay, and the energy of the antineutrino events is on the average less than neutrino events. Owing to the rapid falloff with energy of the antineutrino data and the need to combine antineutrino and neutrino data to obtain structure functions, the analysis that follows has been restricted to the energy range  $20 < E < 220$  GeV. Neutrino data above 220 GeV will be reported in a later paper.

The  $P_\mu$  spectra of Fig. 13 clearly illustrate the minimum muon momentum requirement at  $\sim 4$  GeV/c. The average values of  $P_\mu$  associated with Fig. 13 are

$$\frac{\langle P_\mu \rangle_\nu}{\langle E_\nu \rangle} = 0.54 \pm 0.05, \quad \frac{\langle P_\mu \rangle_{\bar{\nu}}}{\langle E_{\bar{\nu}} \rangle} = 0.68 \pm 0.07. \quad (4.1)$$

Of note in Fig. 14 is that most events have a muon angle less than 300 mrad, well within the angular acceptance ( $\sim 400$  mrad) of the detector. Neutrino events have, on the average, more energy deposited at the hadron vertex than do antineutrino events, as shown in Fig. 15 and indicated by the fractions

$$\frac{\langle E_H \rangle_\nu}{\langle E_\nu \rangle} = 0.46 \pm 0.05, \quad \frac{\langle E_H \rangle_{\bar{\nu}}}{\langle E_{\bar{\nu}} \rangle} = 0.32 \pm 0.03. \quad (4.2)$$

TABLE I. Average values of the parameters associated with the distributions plotted in Figs. 12 to 17.

Quantity	Average values	
	$\nu$	$\bar{\nu}$
$E_\nu$ (GeV)	97	69
$P_\mu$ (GeV)	52	47
$\theta_\mu$ (mrad)	83	56
$E_H$ (GeV)	45	23
$W^2$ (GeV <sup>2</sup> )	65	35
$Q^2$ (GeV <sup>2</sup> )	20	8.2

## D. Monte Carlo comparison

The solid curves shown in Figs. 12–17 are obtained by combining the acceptance and resolution calculations described in Sec. IV B, and serve to illustrate the consistency between the data and the Monte Carlo representation of it. Considering the variety of experimental conditions represented by the data, the ability of the Monte Carlo calculation to model the data sample is good. It is of special interest that the only variable in which a difference between calculation and data is noticeable is  $Q^2$ ; the data exhibit steeper  $Q^2$  distributions. This is due to the scale-invariance violation in the data (see later) which is not put into the Monte Carlo calculation. In modeling the acceptance and resolution these differences in the  $Q^2$  behavior had a negligible effect.

## E. Normalization

In this experiment absolute neutrino and antineutrino fluxes and hence absolute total cross sections were not measured. We obtain differential cross sections from the observed event distributions in  $x$  and  $y$  by means of the relation  $(1/N)(dN/dx dy) = (1/\sigma)(d\sigma/dx dy)$ , and by using a recent compilation of  $\nu$  and  $\bar{\nu}$  total-cross-section data<sup>12</sup> which is displayed in Fig. 18. The total cross sections were taken to be

$$\sigma_\nu = (0.63 \pm 0.02) E_\nu \times 10^{-38} \text{ cm}^2/\text{GeV}, \quad (4.3)$$

$$\sigma_{\bar{\nu}} = (0.30 \pm 0.01) E_{\bar{\nu}} \times 10^{-38} \text{ cm}^2/\text{GeV},$$

which are the best fits to the data above 20 GeV in Fig. 18. We emphasize that the shapes of the differential cross sections and the  $x$  and  $Q^2$  dependences of the structure functions obtained by this method of normalization depend only on the ratio  $\sigma_\nu/\sigma_{\bar{\nu}}$  and not on the absolute values of  $\sigma_\nu$  or  $\sigma_{\bar{\nu}}$ .

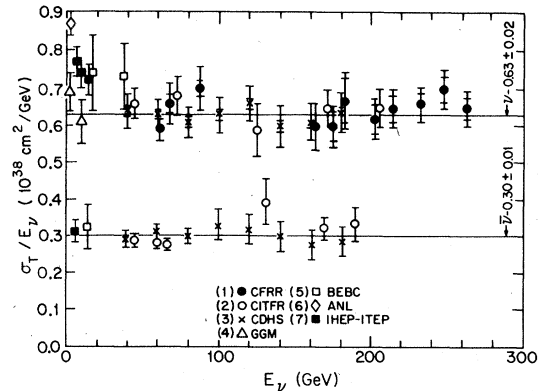


FIG. 18. Summary of neutrino and antineutrino total-cross-section measurements from Ref. 12.

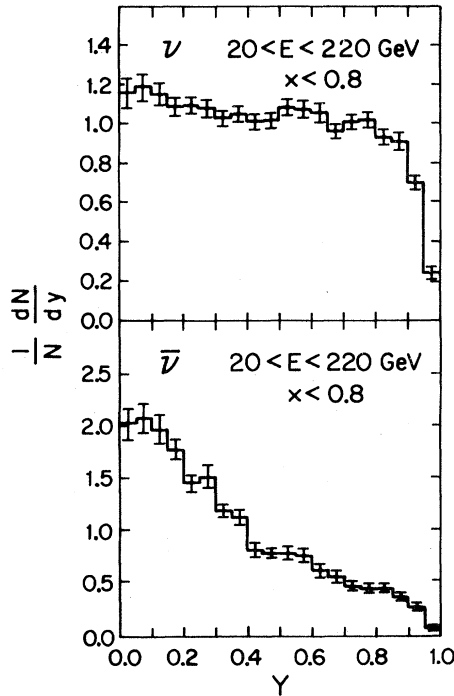


FIG. 19.  $y$  distributions for neutrino and antineutrino events in the energy range  $20 < E < 220$  GeV. An  $x$  cut of 0.8 has been applied to remove quasielastic events.

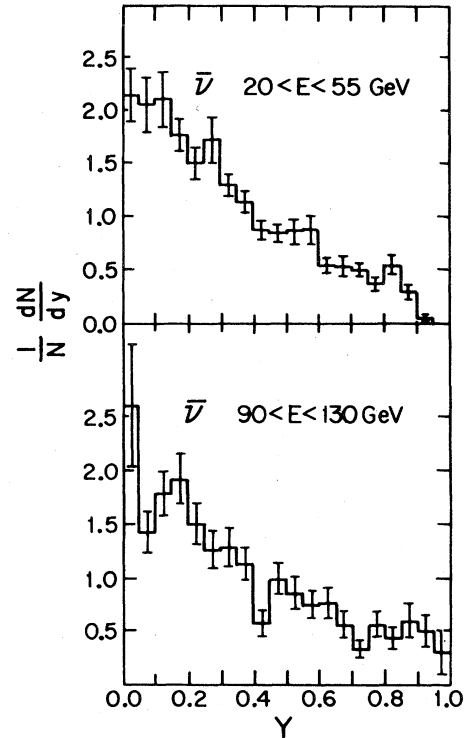


FIG. 21.  $y$  distributions for antineutrino events at low and high energy.

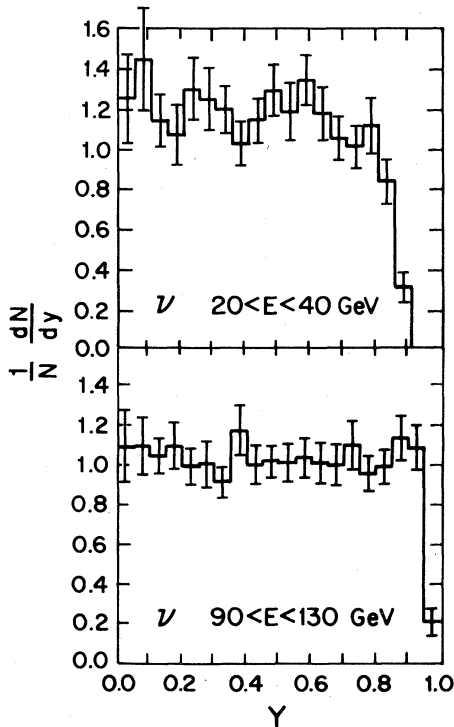


FIG. 20.  $y$  distributions for neutrino events at low and high energy.

#### F. $y$ distributions

The  $y$  distributions for neutrinos and antineutrinos (uncorrected for resolution smearing) in the full energy range  $20 < E < 220$  GeV are given in Fig. 19. The shape parameters for the distributions are  $B^\nu = 0.74 \pm 0.08$  for neutrinos (see below) and  $B^{\bar{\nu}} = 0.72 \pm 0.02$  for antineutrinos. The effect of the radiative corrections applied to the  $y$  distributions was to lower the value for  $B^\nu$  by  $\sim 15\%$  and raise the value of  $B^{\bar{\nu}}$  by  $\sim 5\%$ . Figures 20 and 21 show the neutrino and antineutrino  $y$  distributions in two energy intervals. Tables II and III give the values of the parameters of  $y$  distributions for neutrinos and antineutrinos in five en-

TABLE II. Values of the parameters associated with the antineutrino  $y$  distributions in five energy intervals. Note the increase of the antiquark momentum fraction,  $\frac{1}{2}(1 - B^{\bar{\nu}})$ , with increasing energy.

$E^{\bar{\nu}}$ (GeV)	$\langle E^{\bar{\nu}} \rangle$ (GeV)	$B^{\bar{\nu}}$	$\langle y \rangle$	$\frac{1}{2}(1 - B^{\bar{\nu}})$	$\langle Q^2 \rangle$ (GeV <sup>2</sup> )
20-55	39	$0.77 \pm 0.04$	0.320	$0.12 \pm 0.02$	4.6
55-70	62	$0.74 \pm 0.05$	0.327	$0.13 \pm 0.02$	7.5
70-90	79	$0.71 \pm 0.05$	0.334	$0.14 \pm 0.02$	9.2
90-130	107	$0.68 \pm 0.05$	0.341	$0.16 \pm 0.02$	12
130-220	159	$0.67 \pm 0.05$	0.343	$0.16 \pm 0.02$	20

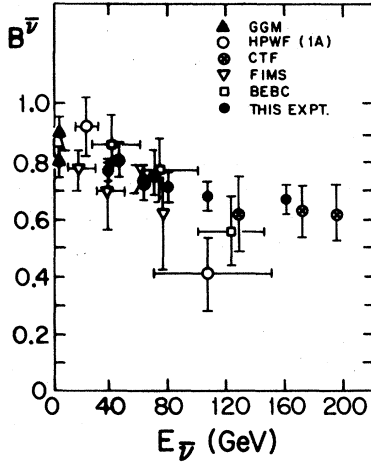


FIG. 22. The shape parameter ( $B^\nu$ ) for antineutrino  $y$  distributions as a function of energy. Data from other experiments are from Ref. 13.

ergy intervals. The values of  $B^\nu$  in Table II show a clear dependence on energy, and indicate a 13% drop in  $B^\nu$  in going from low to high energy as illustrated in Fig. 22. We emphasize that the best fit to the antineutrino  $y$  distributions is, within measurement errors, independent of the value of  $R$  [see Eq. (2.10)]. Hence the values of  $B^\nu$  in Table II are fully corrected and insensitive to the actual value of  $R$ . On the other hand, fits to the neutrino  $y$  distributions reflect a strong correlation between  $B^\nu$  and  $R$ , and therefore the values of  $B^\nu$  in Table II, which have been obtained assuming  $R=0$ , are significantly lower than they would be if  $R$  were taken to be nonzero. This statement applies also to the value of  $B^\nu$  over the entire energy interval 20 to 220 GeV. Data from other experiments have been plotted in Fig. 22 for comparison.<sup>13</sup> The decrease in  $B^\nu$  with energy may be attributed to a combination of charmed-hadron

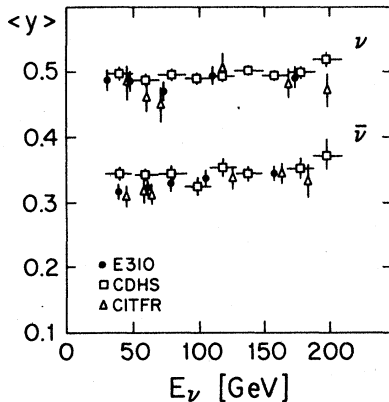


FIG. 23. Average values of  $y$  for antineutrino-induced events as a function of energy. Data from other experiments are from Ref. 14.

TABLE III. Values of the parameters associated with the neutrino  $y$  distributions in five energy intervals. See text for cautionary remarks on the values of  $B^\nu$ .

$E^\nu$ (GeV)	$B^\nu$	$\langle y \rangle$	$\langle E^\nu \rangle$ (GeV)	$\langle Q^2 \rangle$ (GeV <sup>2</sup> )
20–40	$0.85 \pm 0.24$	0.493	31	6.5
40–55	$0.78 \pm 0.21$	0.490	48	10.5
55–90	$0.53 \pm 1.2$	0.477	71	15
90–130	$0.96 \pm 0.22$	0.498	108	22.5
130–220	$0.79 \pm 0.17$	0.491	171	35.5

production and intrinsic scale-breaking effects. Figure 23 shows a corresponding plot of  $\langle y \rangle$  as a function of energy.<sup>14</sup> From these data and Eq. (2.24) the antiquark momentum fraction as a function of energy can be determined and is also shown in Table II. Utilizing  $\bar{\nu}$  dimuon data from this experiment,<sup>15</sup> separate values for  $\int x [\bar{s}(x) dx] / \int x [u(x) + d(x)] dx$  and  $\int x [\bar{u}(x) + \bar{d}(x)] dx / \int x [u(x) + d(x)] dx$  can be obtained and are tabulated in Table IV.

Figures 24 and 25 present the  $y$  distributions for neutrinos and antineutrinos in the energy interval  $20 < E < 220$  GeV for various regions of  $x$ . In the QPM the antineutrino  $y$  distribution at low  $x$  is heavily influenced by the antiquarks in the sea. The  $y$  distribution at high  $x$  is not influenced by antiquarks since the  $x$  distribution of antiquarks is zero for  $x > 0.5$ . The antineutrino data show this behavior clearly. The  $y$  distributions at low  $x$  are much flatter than the distributions at higher  $x$  which exhibit almost a pure  $(1-y)^2$  behavior. The effect for neutrinos is expected to be much smaller and is not observed.

#### G. $x$ distributions

Figure 26 shows the neutrino and antineutrino  $x$  distributions for the full energy range  $20 < E < 220$  GeV. Figures 27 and 28 break the distributions into six energy intervals. A definite deviation from scaling is visible in the dependence on energy of both neutrino and antineutrino  $x$  distributions. Corrections for resolution smearing do not eliminate this behavior. Figure 29 shows an overlay of the fits in three of the six energy intervals as an aid in illustrating the energy dependence.<sup>16</sup>

#### H. $\langle Q^2 \rangle / E$

In the limit of valid scaling,  $\langle Q^2 \rangle = 2ME_{\nu, \bar{\nu}} \langle xy \rangle$ , hence the ratio  $\langle Q^2 \rangle / E_{\nu, \bar{\nu}}$  should be independent of energy.  $\langle Q^2 \rangle / E_{\nu, \bar{\nu}}$  depends solely on the properties of the outgoing muon for fixed  $E_{\nu, \bar{\nu}}$ , since

$$\frac{\langle Q^2 \rangle}{E} = 2M \langle y \rangle = 2M \left\langle \frac{P_\mu}{M} (1 - \cos \theta_{\mu\nu}) \right\rangle. \quad (4.4)$$

TABLE IV. Energy dependence of integrals over antiquark momentum distributions obtained from  $\bar{\nu}$  dimuon data from this experiment and values of  $B^{\bar{\nu}}$  in Table II. Column 4 is column 2 divided by the sum of columns 2 and 3. We have neglected the charmed-quark contribution to the denominators in the headings of columns 2 and 3.

Energy range (GeV)	$\frac{\int x \bar{s}(x) dx}{\int x [\bar{u}(x) + \bar{d}(x)] dx}$	$\frac{\int x [\bar{u}(x) + \bar{d}(x)] dx}{\int x [\bar{u}(x) + \bar{d}(x)] dx}$	$\frac{\int x \bar{s}(x) dx}{\int x [\bar{u}(x) + \bar{d}(x) + \bar{s}(x)] dx}$
$40 < E < 80$	$0.015 \pm 0.005$	$0.12 \pm 0.03$	$0.11 \pm 0.04$
$80 < E < 150$	$0.030 \pm 0.010$	$0.13 \pm 0.04$	$0.19 \pm 0.06$
Full range			
$20 < E < 220$	$0.020 \pm 0.005$	$0.12 \pm 0.03$	$0.14 \pm 0.05$

Values for  $\langle Q^2 \rangle / E$  have been calculated in several energy bins for both neutrinos and antineutrinos and are plotted against energy in Fig. 30 and tabulated in Table V. In calculating  $\langle Q^2 \rangle$  an  $x$  cut of 0.8 was imposed on the data to remove almost all quasielastic events, and the data were corrected for the effect of that cut as well as for acceptance effects using the structure functions measured in this experiment. The corrections were about 20% at the lowest energy and fell rapidly to zero at the highest energy.

Figure 30 shows a drop in  $\langle Q^2 \rangle / E$  with energy rather than the constant behavior required by scale invariance. Data from other experiments are shown in Fig. 30.<sup>17</sup> If the drop in  $\langle Q^2 \rangle / E$  with energy is attributed solely to a finite-mass  $W$  boson, a lower limit of 20 GeV can be placed on the boson mass. Clearly, this limit is small because of the presence of the scale-invariance violation. Systematic errors in  $\langle Q^2 \rangle / E$  have been estimated at  $\pm 5\%$  for both neutrino- and antineutrino-induced interactions.

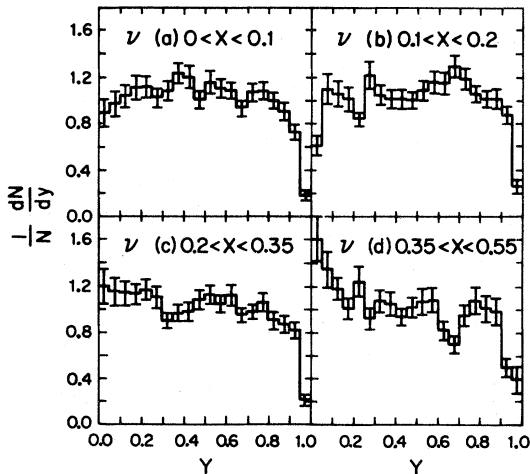


FIG. 24.  $y$  distributions for neutrinos in several intervals of  $x$ .

#### I. Nucleon structure functions; energy and $x$ dependence

$$2xF_1(x)$$

From the  $y$  distributions in Fig. 19 and the total cross sections in Fig. 18 we form the sum of the differential cross sections  $(\frac{1}{2}\pi/G^2ME)(d\sigma^{\nu}/dy + d\sigma^{\bar{\nu}}/dy)$ , which is plotted in Fig. 31. Using Eqs. (2.19)–(2.21) and taking  $\Delta B = B^{\nu} - B^{\bar{\nu}} = 0.07$  (see below), we obtain

$$\langle R \rangle = \sigma_S / \sigma_T = 0.11 \pm 0.04 (\pm 0.03) \quad (4.5)$$

averaged over the energy interval  $20 < E < 220$  GeV, after corrections for radiative and resolution effects. The error in parentheses represents our estimate of the systematic uncertainty in  $\langle R \rangle$ .

Recall that in  $y$  distributions of  $\nu$  and  $\bar{\nu}$  events,  $R$  is strongly correlated with  $B^{\nu}$  but not with  $B^{\bar{\nu}}$ . Hence an accurate value of  $\Delta B$  is difficult to obtain from  $y$  distributions alone. The value  $\Delta B = 0.07$  was found from data on  $B^{\bar{\nu}}$  (Table II) and independent data on antineutrino-induced dimuon produc-

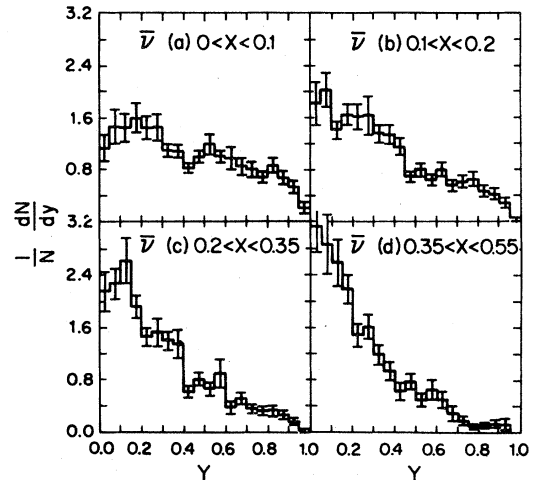


FIG. 25.  $y$  distributions for antineutrinos in several intervals of  $x$ . Note the strong  $x$  dependence due to the peaking of the antiquark fractional momentum distribution at low  $x$ .

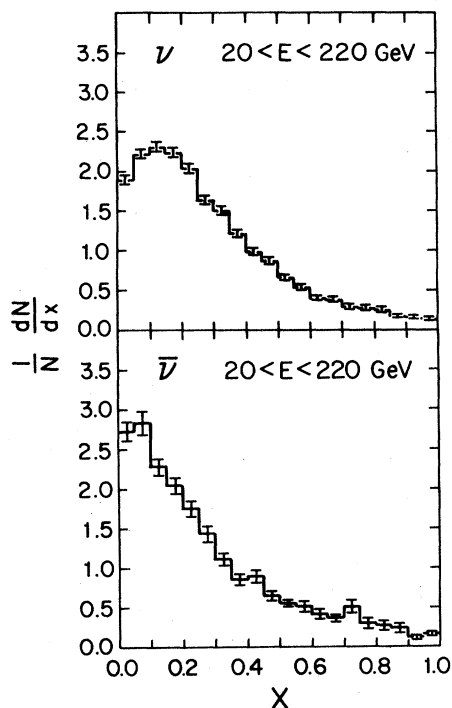


FIG. 26.  $x$  distributions for neutrino and antineutrino events in the energy range  $20 < E < 220$  GeV.

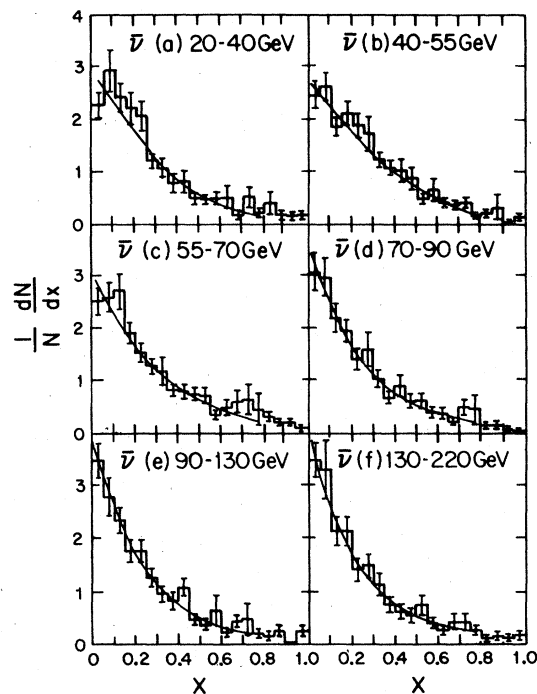


FIG. 28.  $x$  distributions for antineutrino events in six energy intervals. The smooth curves are fits to the form  $ax^\gamma(1-x)^\alpha + b(1-x)^\delta$  for  $x < 0.8$ .

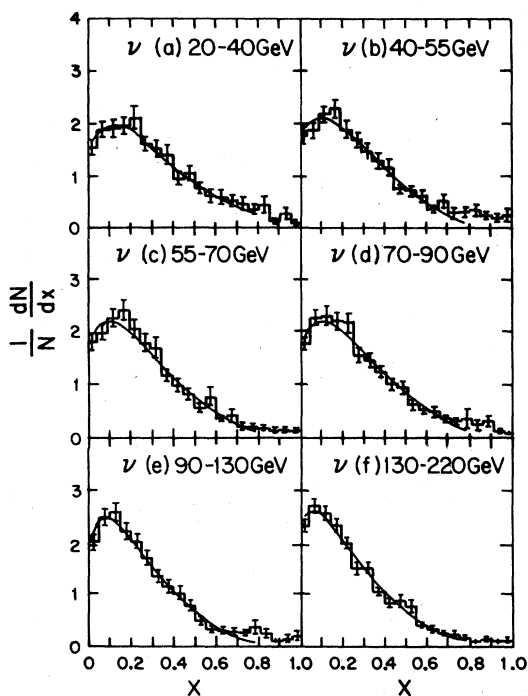


FIG. 27.  $x$  distributions for neutrino events in six energy intervals. The smooth curves are fits to the form  $ax^\gamma(1-x)^\alpha + b(1-x)^\delta$  for  $x < 0.8$ .

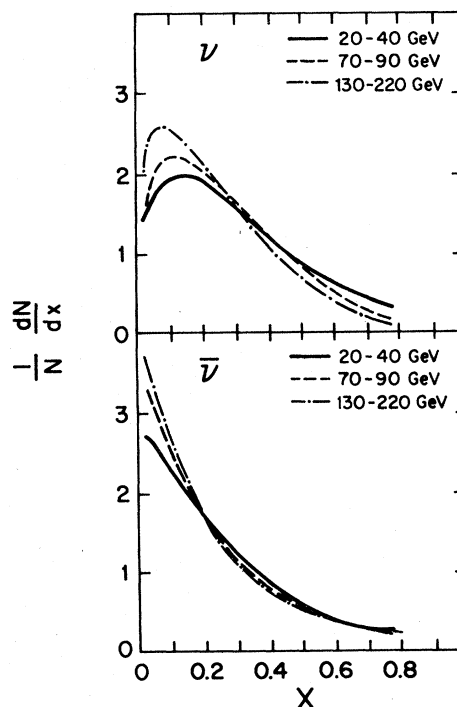


FIG. 29. Overlays of the smooth curves in three of the energy intervals of Figs. 27 and 28 to exhibit the energy dependence of the  $x$  distributions.

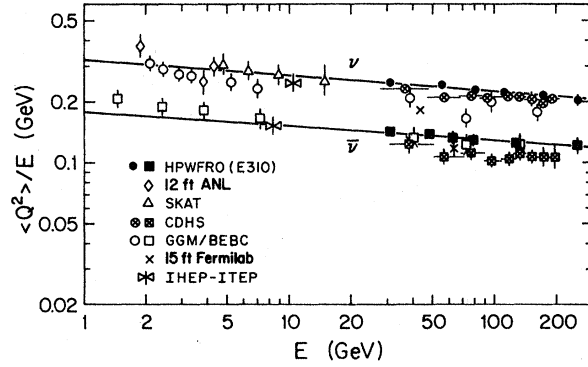


FIG. 30. Plots of  $\langle Q^2 \rangle / E$  as a function of energy for neutrino and antineutrino events. The values have been corrected for resolution smearing. The results of this experiment are given [Harvard-Pennsylvania-Wisconsin-Fermilab-Rutgers-Ohio State (HPWFRO)]. Other data are from Ref. 17. The lines are fits to the data of this experiment (see Table V).

tion<sup>5</sup> (Table IV) which together fix the value of  $\int x \bar{s}(x) dx$  without recourse to neutrino  $y$ -distribution data. The relationship between  $\langle R \rangle$  and  $\Delta B$  is approximately linear over the region  $0 \leq \langle R \rangle \leq 0.3$  with a slope  $\Delta \langle R \rangle / \Delta (\Delta B) = 1.0$ .

We attempted to repeat this procedure in sub-intervals of  $x$  and  $E$  to determine the dependence of  $R$  on those variables. The plot of  $R$  against  $x$  showed erratic behavior strongly influenced by uncertainties in the values of  $\Delta B$  and the resolution smearing corrections. The plot of  $R$  against  $E$  was less erratic but the errors again dominated the result. Thus, systematic uncertainties in the required corrections combined with the small numerical value of  $R$  did not allow reliable, precise information on the  $x$  and  $E$  dependence of  $R$  to be extracted from the data of this experiment.

These difficulties are also inherent to a significant extent in the measurement of  $\langle R \rangle$  for which there is a broad dispersion of the experimental values available at present. Data from inclusive

TABLE V. Values of  $\langle Q^2 \rangle / E$  plotted in Fig. 30. Fits to the form  $\langle Q^2 \rangle / E = A E^\xi$  yield  $A_\nu = 0.32 \pm 0.02$  and  $\xi_\nu = -0.076 \pm 0.015$ ;  $A_{\bar{\nu}} = 0.19 \pm 0.01$ ,  $\xi_{\bar{\nu}} = -0.087 \pm 0.017$ . A fit to a common slope (shown in Fig. 30) gives  $A_\nu = 0.33 \pm 0.01$ ,  $A_{\bar{\nu}} = 0.18 \pm 0.01$ , and  $\xi = -0.079 \pm 0.010$ .

$E$ (GeV)	$\nu$ $\langle Q^2 \rangle / E$ (GeV)	$E$ (GeV)	$\bar{\nu}$ $\langle Q^2 \rangle / E$ (GeV)
20–40	$0.246 \pm 0.012$	20–40	$0.141 \pm 0.007$
40–70	$0.243 \pm 0.012$	40–55	$0.139 \pm 0.007$
70–90	$0.228 \pm 0.011$	55–70	$0.132 \pm 0.007$
90–130	$0.225 \pm 0.011$	70–90	$0.129 \pm 0.006$
130–220	$0.218 \pm 0.011$	90–220	$0.124 \pm 0.006$
220–325	$0.199 \pm 0.010$	220–325	$0.120 \pm 0.006$

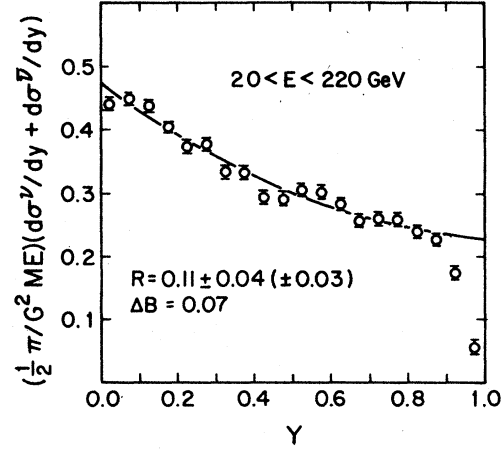


FIG. 31. Data for the extraction of  $\langle R \rangle$  in the energy range  $20 < E < 220$  GeV.

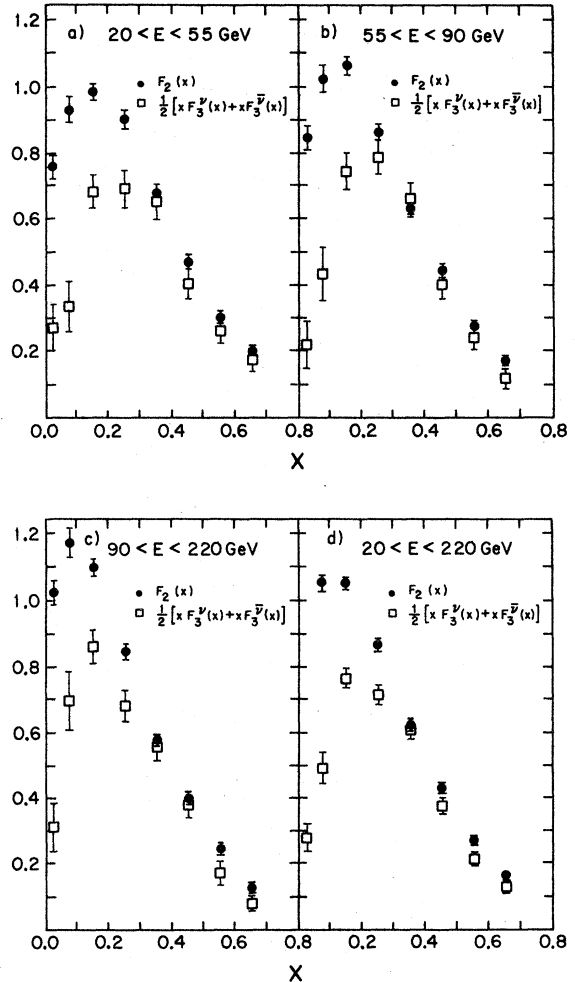


FIG. 32.  $F_2(x)$  and  $\frac{1}{2}[x F_3^\nu(x) + x F_3^{\bar{\nu}}(x)]$  in the energy interval  $20 < E < 220$  GeV and in three smaller energy intervals.



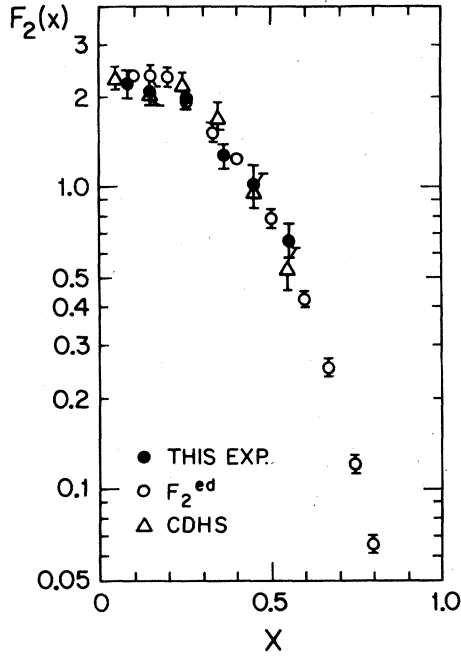


FIG. 33. Comparison of  $F_2(x)$  in the energy range  $20 < E < 30$  GeV from this experiment with  $e$ - $d$  data [Ref. 19]. Also plotted is  $F_2^{Fe}(x)$  from the CDHS experiment [Ref. 12] in the same energy range. All distributions are normalized to  $\int F_2(x) dx = 1$ .

electron scattering experiments<sup>18</sup> on hydrogen yield  $\langle R \rangle = 0.21 \pm 0.10$  over the kinematic range  $3 < Q^2 < 18$  GeV<sup>2</sup>, and no appreciable dependence of  $R$  on  $x$  or  $Q^2$ . Other neutrino data from de Groot *et al.*,<sup>12</sup> corrected for radiative and resolution effects and in the energy interval  $30 < E < 200$  GeV gave  $\langle R \rangle = 0.03 \pm 0.05$ . Two results from neutrino

data presented *without radiative corrections* are  $\langle R \rangle = 0.20 \pm 0.11$  from the CITFR group<sup>18</sup> and  $\langle R \rangle = 0.15 \pm 0.10$  ( $\pm 0.04$ ) from the Gargamelle-BEBC collaboration.<sup>18</sup>

#### $F_2(x)$ and $x F_3(x)$

The structure functions  $F_2(x)$  and  $x F_3(x)$  have been extracted according to the prescription in Eqs. (2.17) and (2.18) in the region  $20 < E < 220$  GeV, and also in three smaller energy intervals. The results, given in Fig. 32, have been corrected for radiative and resolution effects, and regions at large  $x$ , where resolution corrections exceed 30%, have been omitted. No correction has been made to the data in Fig. 32 to take into account the nonzero value of  $R$ . As expected from the  $x$  distributions in Figs. 27 and 28, both  $F_2(x)$  and  $x F_3(x)$  show a decrease in  $\langle x \rangle$  with increasing neutrino energy or, equivalently, increasing  $\langle Q^2 \rangle$ , i.e., a clear violation of scale invariance similar to that observed in charged lepton production experiments.<sup>19</sup>

We show in Fig. 33 a comparison of our neutrino data in the energy interval  $20 < E < 30$  GeV and low-energy data from another high-statistics neutrino experiment<sup>12</sup> with electroproduction data (Riordan *et al.*, Ref. 19) on the shape of  $F_2(x)$ . The agreement among all experiments is good.

We have fitted the valence-quark momentum distributions  $\frac{1}{2}[x F_2^v(x) + x F_3^v(x)]$  in Fig. 32 to a function of the form  $V x^\gamma (1-x)^\alpha$ , as suggested in both the QPM and QCD. The results are tabulated in Table VI. We remark that more than 50% of the contribution to the integral  $\int x F_3(x) dx/x$ , the total number of valence quarks, comes from the first bin in  $x$ , for which uncertainties due to corrections

TABLE VI. Summary of parameters for valence-quark and antiquark distributions. The valence-quark distributions have been fit to the form  $V x^\gamma (1-x)^\alpha$ ; the antiquark distributions to the form  $D(1-x)^\delta$ .

Valence quarks				
	$V$	Fit in full $x$ range		$\alpha$
		$\gamma$		
$20 < E < 55$ GeV	$5.5 \pm 0.2$	$0.86 \pm 0.03$		$3.1 \pm 0.1$
$55 < E < 90$ GeV	$7.4 \pm 0.5$	$0.90 \pm 0.04$		$3.6 \pm 0.2$
$90 < E < 220$ GeV	$6.2 \pm 1.6$	$0.74 \pm 0.10$		$3.8 \pm 0.3$
$20 < E < 220$ GeV	$6.1 \pm 1.0$	$0.82 \pm 0.07$		$3.40 \pm 0.02$
Antiquarks				
	Method 1 $\nu, \bar{\nu};$ all $y$		Method 2 $\bar{\nu}; 0.7 < y < 0.9$	
	$D$	$\delta$	$D$	$\delta$
$20 < E \leq 55$ GeV	$0.34 \pm 0.04$	$4.7 \pm 0.7$	$0.52 \pm 0.07$	$7.1 \pm 0.9$
$55 < E < 90$ GeV	$0.46 \pm 0.05$	$7.2 \pm 1.0$	$0.59 \pm 0.10$	$9.1 \pm 1.1$
$90 < E < 220$ GeV	$0.48 \pm 0.06$	$7.3 \pm 1.2$	$0.89 \pm 0.12$	$13.4 \pm 1.4$
$20 < E < 220$ GeV	$0.41 \pm 0.03$	$6.0 \pm 0.5$	$0.62 \pm 0.05$	$8.0 \pm 0.6$

are largest. A small variation in that bin has a very large effect on the value of the number of valence quarks indicated by the data, as illustrated in Fig. 34. As a consequence, it is difficult to make a precise quantitative comparison of the experimental value of the valence-quark content of the nucleon with the value suggested by QCD.

#### J. Antiquark momentum distributions

We obtain directly from Fig. 32 and Eq. (2.22) the fractional momentum distributions for antiquarks in the combination  $(\bar{u} + \bar{d} + \frac{3}{2}\bar{s} + \frac{1}{2}\bar{c})$  in several energy intervals; these are shown in Fig. 35 and Table VI. The  $x$  distributions of antineutrinos at high  $y$ ,  $0.7 < y < 0.9$ , yield the fractional momentum distributions of a similar but not identical antiquark combination  $(\bar{u} + \bar{d} + 2\bar{s})$  [see Eq. (2.23)], which are also included in Fig. 35 and Table VI. These distributions show sharp peaking at very low  $x$  and fall rapidly to zero at  $x \geq 0.5$ . The difference at low  $x$  between the two sets of antiquark distributions in Fig. 35 may be a consequence of the different  $\langle Q^2 \rangle$  regions represented in the two methods of extraction. In Fig. 35, we have in addition plotted the antiquark momentum fraction in the energy interval  $20 < E < 220$  GeV obtained from  $\frac{1}{2}(1 - B^{\bar{\nu}})$  and Eq. (2.24), i.e., from antineutrino  $y$ -distribution data. The agreement among the results found by these different methods is satisfactory.

In Fig. 36 is shown a comparison of the antiquark fractional momentum distribution  $x[\bar{u}(x) + \bar{d}(x) + \frac{3}{2}\bar{s}(x) + \frac{1}{2}\bar{c}(x)]$  with the corresponding distribution for strange antiquarks  $x\bar{s}(x)$  obtained

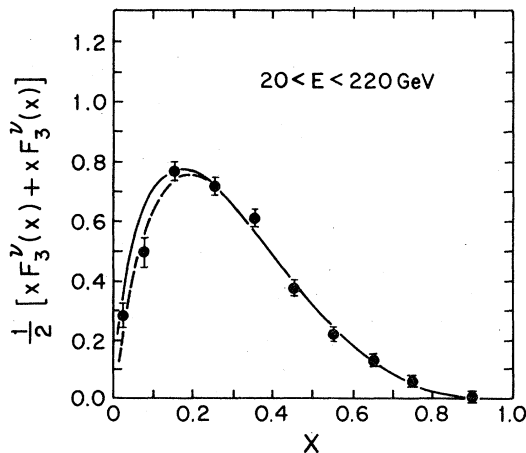


FIG. 34. Illustration of the sensitivity of the valence-quark counting procedure to the data at low  $x$ . The curves are fits of the form  $Vx^\gamma(1-x)^\alpha$ . The solid curve is fitted for  $x > 0.10$ ; the dashed curve for  $x > 0.05$ . The former yields  $\int q_v(x)dx = 2.5 \pm 0.4$  while the latter gives  $2.1 \pm 0.4$ .

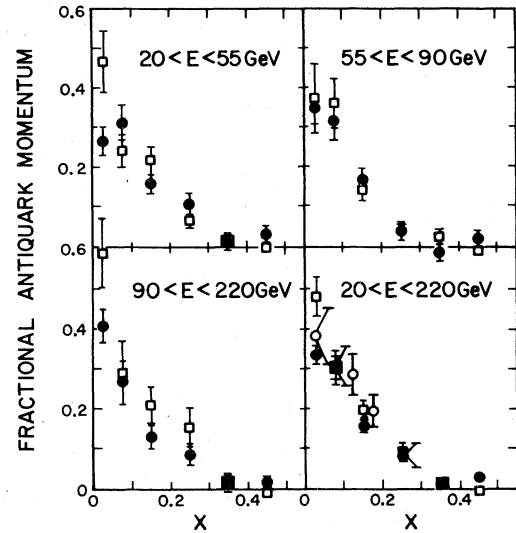


FIG. 35. Fractional antiquark momentum distributions in the energy interval  $20 < E < 220$  GeV, and in three smaller energy intervals. Solid circles are  $x[\bar{u}(x) + \bar{d}(x) + \frac{3}{2}\bar{s}(x) + \frac{1}{2}\bar{c}(x)]$  from neutrino and antineutrino  $x$  distributions at all  $y$ . Open squares are  $x[\bar{u}(x) + \bar{d}(x) + 2\bar{s}(x)]$  from antineutrino  $x$  distributions at high  $y$  ( $0.7 < y < 0.9$ ). The distribution derived from  $\frac{1}{2}(1 - B^{\bar{\nu}})$ , i.e., from antineutrino  $y$  distributions at all  $x$ , in the energy region  $20 < E < 220$  GeV is plotted as open circles. See also Tables II, IV, and VI.

from data on antineutrino-induced dimuons from this experiment. The latter distribution is simply the observed  $x$  distribution of  $\bar{\nu}$ -induced dimuon events after correction for apparatus acceptance and pion and kaon decays in flight, but with no correction for the escape of the final-state antineutrino. The similarity in shape is striking.

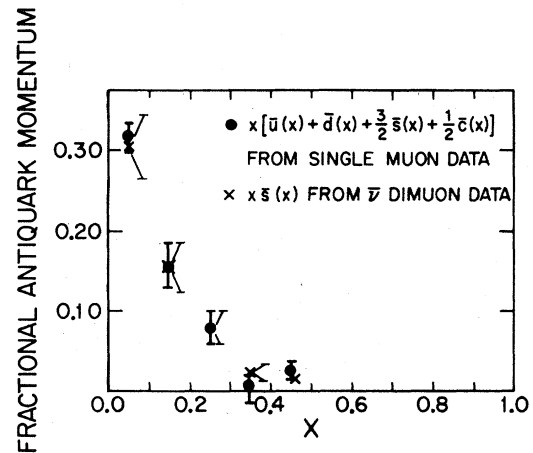


FIG. 36. Comparison of the antineutrino distribution  $x[\bar{u}(x) + \bar{d}(x) + \frac{3}{2}\bar{s}(x) + \frac{1}{2}\bar{c}(x)]$  derived from single-muon data with the observed  $x$  distribution  $[x\bar{s}(x)]$  for antineutrino-induced dimuons from this experiment. The latter distribution is normalized to the area of the former.

### K. Nucleon structure functions; $x$ and $Q^2$ dependence

To obtain from the data the explicit dependence of the structure functions on  $x$  and  $Q^2$  is more difficult than to find the dependence on the experimental variables  $x$  and  $E_\nu$ . To go directly to  $Q^2$  as one of the variables requires detailed knowledge of the neutrino and antineutrino flux shapes.

$$\frac{d\sigma^{\nu, \bar{\nu}}(x, E_H, E_\nu)}{dx dE_H} = \frac{G^2 M}{\pi} \left\{ \left(1 - \frac{E_H}{E_\nu}\right) F_2(x, E_H) + x \left(\frac{E_H}{E_\nu}\right)^2 F_1(x, E_H) \pm \left[ \left(\frac{E_H}{E_\nu}\right) - \frac{1}{2} \left(\frac{E_H}{E_\nu}\right)^2 \right] x F_3(x, E_H) \right\}, \quad (4.6)$$

where now with the change of variables the simple factorization in terms of the variables  $x$ ,  $y$ , and  $E_\nu$  is lost. Experimentally, we measure the event distribution  $dN/dx dE_H$  which, for fixed  $E_H$ , is related to the differential cross section by

$$\frac{dN}{dx dE_H} = \int_{E_{\min}}^{E_{\max}} K \phi(E) \frac{d\sigma(x, E_H, E)}{dx dE_H} dE, \quad (4.7)$$

where  $\phi(E)$  is the neutrino (antineutrino) flux and  $K$  specifies the detector properties (mass, size, etc.). The limits  $E_{\min}$  and  $E_{\max}$  represent the neutrino (antineutrino) energies that are accessible for the given value of  $E_H$ . Hence the number of events observed as a function of  $x$  for fixed  $E_H$  is

$$\frac{dN^{\nu, \bar{\nu}}}{dx dE_H} = \frac{G^2 M}{\pi} \left[ (\epsilon_1 - \epsilon_2 E_H) F_2(x, E_H) + \epsilon_3 E_H^2 x F_1(x, E_H) \pm \left( \epsilon_2 E_H - \frac{\epsilon_3}{2} E_H^2 \right) x F_3(x, E_H) \right], \quad (4.8)$$

where  $\epsilon_1$ ,  $\epsilon_2$ , and  $\epsilon_3$  are the flux integrals

$$\begin{aligned} \epsilon_1 &= \int_{E_{\min}}^{E_{\max}} K \phi(E) dE, \\ \epsilon_2 &= \int_{E_{\min}}^{E_{\max}} K \phi(E) \frac{dE}{E}, \\ \epsilon_3 &= \int_{E_{\min}}^{E_{\max}} K \phi(E) \frac{dE}{E^2}. \end{aligned} \quad (4.9)$$

Typically,  $(E_{\max} - E_{\min}) \gtrsim 100$  GeV so that  $\epsilon_1$ ,  $\epsilon_2$ , and  $\epsilon_3$  are relatively insensitive to the detailed shape of  $\phi(E)$ . The fluxes  $\phi(E)$  are found from the measured  $\nu$  and  $\bar{\nu}$  event energy spectra by means of the relations

$$K \phi(E + \Delta E) = N(E + \Delta E) / \sigma(E + \Delta E), \quad (4.10)$$

where  $N(E + \Delta E)$  is the corrected number of events observed in the energy interval  $E + \Delta E$ . Equations (4.8)–(4.10) can be solved to find  $F_2(x, Q^2)$  and  $x F_3(x, Q^2)$  with good accuracy.

Events were binned in seven intervals of  $E_H$ , and values of  $F_2(x, E_H)$  and  $x F_3(x, E_H)$  were calculated

However, upon changing to an equivalent set of variables,  $x$  and  $E_H$ , one observes that the calculation of the structure functions is not exceptionally sensitive to the detailed shapes of the neutrino and antineutrino fluxes.  $F_2(x, E_H)$  and  $x F_3(x, E_H)$  can then be expressed as  $F_2(x, Q^2)$  and  $x F_3(x, Q^2)$  using  $Q^2 = 2Mx E_H$ .

The differential cross section can be written in the variables  $x$  and  $E_H$  as

in those intervals. These values were corrected for radiative effects and energy resolution, but no correction was made to  $F_2(x, E_H)$  to account for the small effects due to the nonzero value of  $R$  determined above (Sec. IV I); no correction is necessary for  $x F_3(x, Q^2)$ . Bins in  $x$  where the resolution smearing correction exceeded 30% were excluded. The results are given in Table VII. Changing variables from  $x$  and  $E_H$  to  $x$  and  $Q^2$ , one obtains the results shown in Figs. 37 and 38, and also recorded in Table VII.

This method of extracting  $F_2(x, Q^2)$  and  $x F_3(x, Q^2)$  was checked by a completely independent analysis which generated events in various  $x$  and  $Q^2$  bins according to Eq. (2.5) while setting two of the structure functions to zero and the third to a constant value in alternation. The measured event energy distributions for neutrinos and antineutrinos (Fig. 12) and the resolution function of Fig. 8 were explicitly introduced in the Monte Carlo calculation. By comparing the experimental data with these Monte Carlo samples, after appropriate normalization, one obtains  $F_2(x, Q^2)$  and  $x F_3(x, Q^2)$ . The good agreement between the results obtained by the two methods is evidence that any error introduced by the analysis technique itself is small. Furthermore, we have studied the effects on  $F_2(x, Q^2)$  and  $x F_3(x, Q^2)$  of (a) errors in the  $\nu$  and  $\bar{\nu}$  cross sections and fluxes, (b) systematic errors in the calibrations of the calorimeters and the muon spectrometer, and (c) uncertainties in the corrections for acceptance, resolution smearing, and radiative effects. We conclude that the systematic error in the absolute values of  $F_2(x, Q^2)$  does not exceed  $\pm 12\%$ , while the limit on the corresponding error in  $x F_3(x, Q^2)$  is  $\pm 15\%$  due to the increased sensitivity of the latter quantity to possible errors in the cross sections and fluxes. Within any  $x$  region in the plots of Figs. 37 and 38 the systematic error in the  $Q^2$  dependence is less than or about equal to the indicated statistical error on the points.

The results in Figs. 37 and 38 clearly delineate

TABLE VII. Values of  $F_2(x, Q^2) = F_2(x, 2MxE_H)$  and  $xF_3(x, Q^2) = xF_3(x, 2MxE_H)$  corresponding to the data points in Figs. 37 and 38. The errors are statistical only. The correction is the multiplicative factor that has been applied to remove the effect of resolution smearing.

$E_H$ (GeV)	$x$	$Q^2$ (GeV <sup>2</sup> )	$F_2$	Applied resolution correction	$xF_3$	Applied resolution correction
5- 10	0.0 -0.05	0.36	$0.84 \pm 0.05$	0.94		
	0.05-0.10	1.07	$1.19 \pm 0.07$	0.98	$0.80 \pm 0.35$	0.96
	0.10-0.20	2.13	$1.10 \pm 0.04$	1.03	$1.11 \pm 0.23$	1.05
	0.20-0.30	3.56	$0.93 \pm 0.04$	1.08	$1.15 \pm 0.21$	1.10
	0.30-0.40	4.98	$0.69 \pm 0.04$	1.09	$0.66 \pm 0.19$	1.08
	0.40-0.50	6.40	$0.47 \pm 0.03$	1.05	$0.35 \pm 0.15$	0.98
	0.50-0.60	7.82	$0.28 \pm 0.02$	1.01	$0.41 \pm 0.12$	0.98
	0.60-0.70	9.24	$0.19 \pm 0.02$	0.93		
10- 20	0.0 -0.05	0.70	$1.00 \pm 0.04$	0.91	$0.21 \pm 0.11$	0.76
	0.05-0.10	2.11	$1.22 \pm 0.05$	0.96	$0.52 \pm 0.12$	0.92
	0.10-0.20	4.22	$1.17 \pm 0.03$	1.01	$0.71 \pm 0.08$	1.00
	0.20-0.30	7.04	$0.90 \pm 0.03$	1.07	$0.79 \pm 0.07$	1.07
	0.30-0.40	9.86	$0.70 \pm 0.03$	1.09	$0.67 \pm 0.07$	1.08
	0.40-0.50	12.67	$0.46 \pm 0.02$	1.07	$0.49 \pm 0.06$	1.06
	0.50-0.60	15.49	$0.24 \pm 0.02$	1.03	$0.27 \pm 0.04$	1.01
	0.60-0.70	18.30	$0.14 \pm 0.01$	0.94	$0.12 \pm 0.03$	0.94
20- 30	0.0 -0.05	1.16	$1.03 \pm 0.05$	0.93	$0.38 \pm 0.09$	0.77
	0.05-0.10	3.48	$1.25 \pm 0.05$	0.96	$0.54 \pm 0.10$	0.87
	0.10-0.20	6.97	$1.18 \pm 0.04$	1.00	$0.91 \pm 0.07$	0.98
	0.20-0.30	11.61	$1.00 \pm 0.04$	1.05	$0.89 \pm 0.07$	1.07
	0.30-0.40	16.26	$0.59 \pm 0.03$	1.07	$0.55 \pm 0.05$	1.11
	0.40-0.50	20.90	$0.39 \pm 0.02$	1.08	$0.39 \pm 0.04$	1.11
	0.50-0.60	25.55	$0.23 \pm 0.02$	1.07	$0.20 \pm 0.03$	1.10
	0.60-0.70	30.19	$0.14 \pm 0.02$	1.01	$0.13 \pm 0.03$	1.02
30- 40	0.0 -0.05	1.63	$1.04 \pm 0.05$	0.92	$0.30 \pm 0.08$	0.76
	0.05-0.10	4.90	$1.27 \pm 0.07$	0.95	$0.55 \pm 0.10$	0.88
	0.10-0.20	9.79	$1.14 \pm 0.04$	0.99	$0.95 \pm 0.07$	0.98
	0.20-0.30	16.32	$0.88 \pm 0.04$	1.04	$0.73 \pm 0.06$	1.05
	0.30-0.40	22.85	$0.53 \pm 0.03$	1.07	$0.62 \pm 0.05$	1.08
	0.40-0.50	29.38	$0.41 \pm 0.03$	1.09	$0.45 \pm 0.05$	1.10
	0.50-0.60	35.91	$0.18 \pm 0.02$	1.07	$0.15 \pm 0.03$	1.09
	0.60-0.70	42.44	$0.14 \pm 0.02$	1.01	$0.15 \pm 0.03$	1.01
40- 60	0.0 -0.05	2.30	$1.24 \pm 0.06$	0.94	$0.27 \pm 0.08$	0.79
	0.05-0.10	6.89	$1.33 \pm 0.06$	0.96	$0.64 \pm 0.08$	0.90
	0.10-0.20	13.78	$1.26 \pm 0.04$	0.99	$0.75 \pm 0.06$	0.97
	0.20-0.30	22.97	$0.91 \pm 0.04$	1.04	$0.85 \pm 0.05$	1.03
	0.30-0.40	32.16	$0.57 \pm 0.03$	1.07	$0.54 \pm 0.04$	1.08
	0.40-0.50	41.35	$0.38 \pm 0.02$	1.08	$0.36 \pm 0.03$	1.09
	0.50-0.60	50.54	$0.21 \pm 0.02$	1.06	$0.15 \pm 0.03$	1.09
	0.60-0.70	59.73	$0.14 \pm 0.02$	1.02	$0.14 \pm 0.02$	1.03
60- 90	0.0 -0.05	3.42	$1.39 \pm 0.07$	0.96	$0.23 \pm 0.09$	0.79
	0.05-0.10	10.27	$1.35 \pm 0.07$	0.97	$0.74 \pm 0.09$	0.94
	0.10-0.20	20.53	$1.23 \pm 0.05$	1.00	$1.01 \pm 0.06$	1.00
	0.20-0.30	34.21	$0.80 \pm 0.04$	1.03	$0.74 \pm 0.05$	1.04
	0.30-0.40	42.91	$0.49 \pm 0.03$	1.05	$0.43 \pm 0.04$	1.07
	0.40-0.50	61.59	$0.34 \pm 0.03$	1.07	$0.32 \pm 0.04$	1.10
	0.50-0.60	75.28	$0.15 \pm 0.02$	1.07	$0.12 \pm 0.03$	1.11
	0.60-0.70	88.97	$0.10 \pm 0.02$	1.04	$0.05 \pm 0.02$	1.09

TABLE VII. (Continued)

$E_H$ (GeV)	$x$	$Q^2$ (GeV <sup>2</sup> )	$F_2$	Applied resolution correction	$xF_3$	Applied resolution correction
90-170	0.0-0.05	5.67	$1.54 \pm 0.09$	0.97		
	0.05-0.10	17.00	$1.30 \pm 0.07$	0.97	$0.70 \pm 0.09$	0.93
	0.10-0.20	33.99	$1.18 \pm 0.05$	0.99	$0.81 \pm 0.06$	0.98
	0.20-0.30	56.66	$0.80 \pm 0.04$	1.02	$0.66 \pm 0.05$	1.03
	0.30-0.40	79.32	$0.46 \pm 0.03$	1.06	$0.46 \pm 0.03$	1.07
	0.40-0.50	101.98	$0.34 \pm 0.03$	1.08	$0.33 \pm 0.03$	1.10
	0.50-0.60	124.64	$0.13 \pm 0.03$	1.12	$0.09 \pm 0.02$	1.11
	0.60-0.70	147.30	$0.08 \pm 0.02$	1.09	$0.04 \pm 0.02$	1.16

the  $Q^2$  dependence of  $F_2(x, Q^2)$  and  $xF_3(x, Q^2)$ . For low  $x$  the structure functions rise with increasing  $Q^2$ , remain constant with  $Q^2$  for intermediate values of  $x$ , and fall with increasing  $Q^2$  for large  $x$ . The data from this experiment and from the other high-statistics experiment,<sup>12</sup> which are provided for comparison in Figs. 39 and 40, show excellent quantitative agreement in both  $F_2(x, Q^2)$  and  $xF_3(x, Q^2)$  over the entire range of  $x$  and  $Q^2$ , except possibly in the highest  $x$  region where statistical and systematic errors are largest. We note, however, that the agreement of the absolute values of the structure functions from the two ex-

periments within a given  $x$  interval is less significant (in view of the possible systematic errors of 12-15% mentioned above) than is the agreement of the two experiments of the  $Q^2$  dependence in that  $x$  interval.

#### V. SUMMARY AND CONCLUSIONS

Certain quantities exhibit most directly the strength of the QPM and, simultaneously, an energy dependence which is its weakness. The average inelasticity of the lepton-nucleon interactions

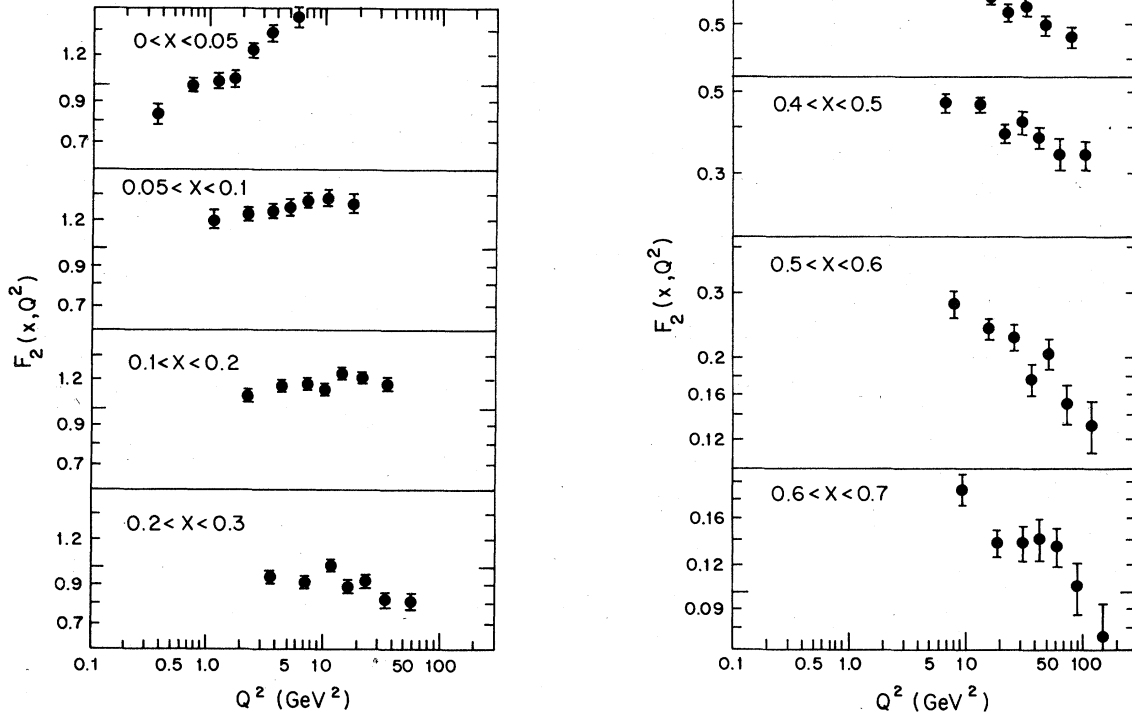


FIG. 37.  $F_2(x, Q^2)$  as a function of  $Q^2$  in eight intervals of  $x$ .

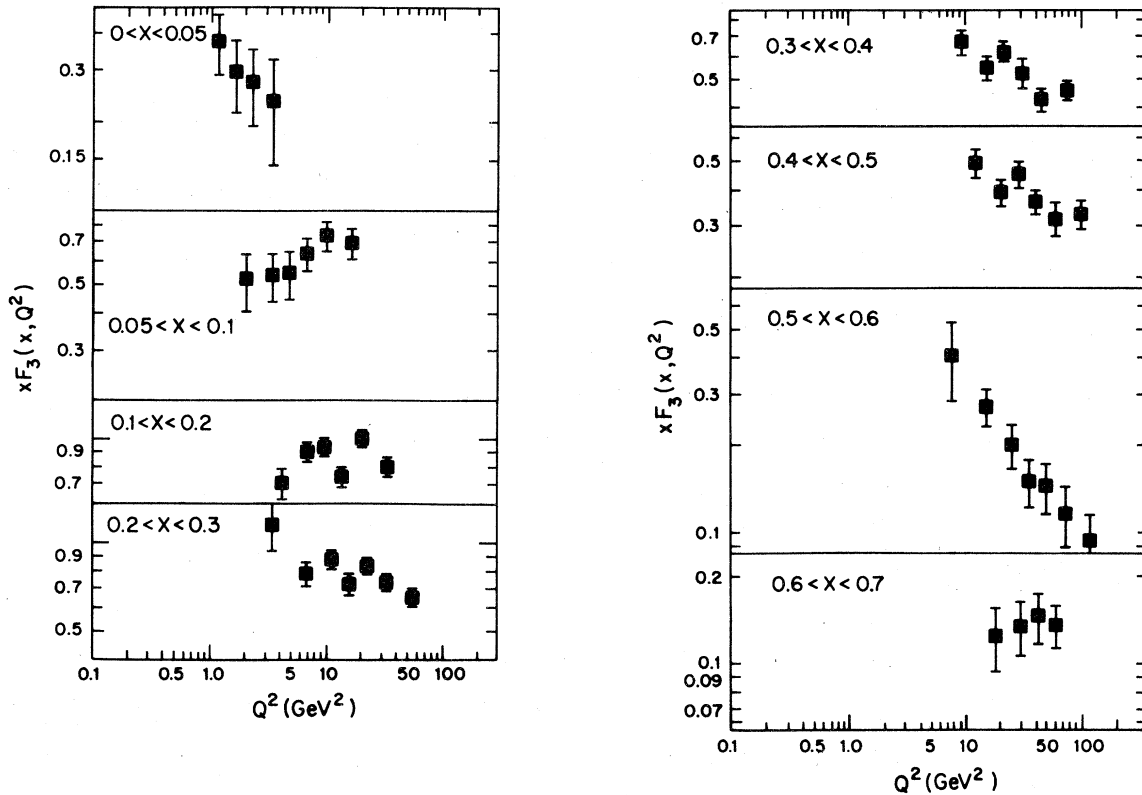


FIG. 38.  $\alpha F_3(x, Q^2)$  as a function of  $Q^2$  in eight intervals of  $x$ .

is one such quantity. The plot of  $\langle y \rangle$  against energy in Fig. 23 shows no energy dependence for  $\nu$ -induced events, as expected in the QPM given the precision of present experiments. The corresponding plot for  $\bar{\nu}$ -induced events shows a small but unmistakable increase of  $\langle y \rangle$  with energy that is consistent with charmed-hadron production and an intrinsic energy dependence of the structure functions. The same effect is manifested in the plot of  $B^{\bar{\nu}}$  against energy in Fig. 22. Similarly, the values of  $\langle x \rangle$  for both  $\nu$  and  $\bar{\nu}$  events in Figs. 27 and 28 show a decrease with increasing energy. A third quantity of interest is  $\langle Q^2 \rangle / E = 2M \langle xy \rangle$  which exhibits a corresponding energy dependence in the  $\nu$  and  $\bar{\nu}$  data of Fig. 30.

The dimensionless variables  $\langle y \rangle$ ,  $\langle x \rangle$ , and  $\langle xy \rangle$  are determined without knowledge of the absolute cross sections or, in the case of  $\langle xy \rangle$ , knowledge of the fluxes. Hence, in addition to exhibiting the breakdown of scale invariance, they serve also as tests for residual small systematic errors in the detection efficiencies, i.e., errors in the treatment of events in certain regions of  $E_H$ ,  $E_\mu$ , and  $\theta_{\mu\nu}$ , in different experiments. Apart from the statistical errors, the data in Figs. 22 and 30

show small systematic differences that are as yet unreconciled. These do not seriously influence the general conclusions that are drawn from present deep-inelastic lepton-nucleon scattering data, but they underline the importance of eliminating such systematic effects in future experiments aimed at much higher precision.

The dependence on  $x$  and  $E$  of the structure functions  $F_2(x)$  and  $\alpha F_3(x)$  is well specified as in Fig. 32, and there is satisfactory agreement among the relatively precise results of different experiments, e.g., as shown in Fig. 33. It is worth noting that the valence-quark distributions in Fig. 32 show a clear decrease of  $\langle x \rangle$  with increasing  $E$ , which could be explained by increased emission of gluons by quarks at higher  $Q^2$  as expected in QCD. It follows that  $F_2(x)$  also shows a similar effect.

On the other hand, detailed quantitative measurements of  $\alpha F_1(x)$  have proved difficult and those that have been done are not completely adequate. The data from which the result of this paper is obtained, i.e.,  $\int_0^1 2xF_1(x)dx = (0.90 \pm 0.04) \int_0^1 F_2(x)dx$  in the energy interval  $20 < E < 220$  GeV, do not permit the extraction of useful information on the

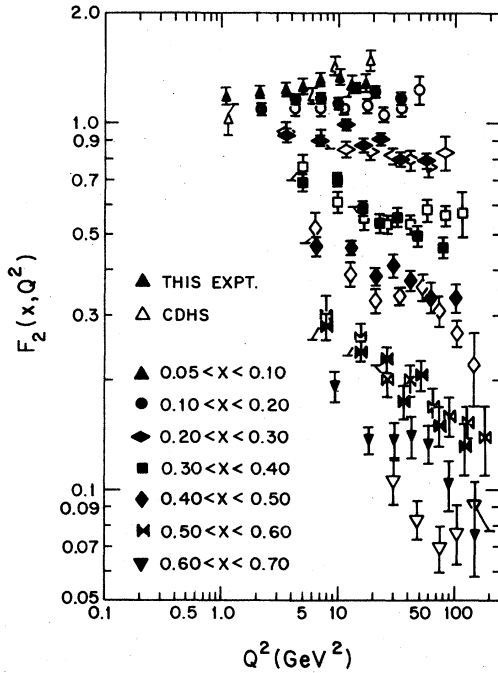


FIG. 39. A comparison of  $F_2(x, Q^2)$  as a function of  $Q^2$  in several intervals of  $x$  from this experiment (solid symbols) and the CDHS experiment (open symbols, Ref. 12). Note the first interval for CDHS is  $0.06 < x < 0.10$ . Three CDHS points are not visible in the figure, two in the interval  $0.06 < x < 0.10$  ( $F_2 = 1.13 \pm 0.07$  at  $Q^2 = 2.25$   $\text{GeV}^2$  and  $F_2 = 1.20 \pm 0.07$  at  $Q^2 = 3.75$   $\text{GeV}^2$ ) and one in the interval  $0.10 < x < 0.20$  ( $F_2 = 1.14 \pm 0.07$  at  $Q^2 = 2.11$   $\text{GeV}^2$ ).

$x$  and  $E$  dependences of  $x F_1(x)$ . Within experimental errors, there is no serious disagreement on the value of  $\langle R \rangle$  among the various existing experiments, but no precise value of  $\langle R \rangle$  can be obtained from the available data at this time. It is an important requirement for future experiments to satisfy this need.

The differential cross sections and structure functions yield the  $x$  and  $E$  dependences of the antiquark momentum distributions. Using the same data, different analyses give substantially similar results as shown in Fig. 35 and Tables II, IV, and VI. Nevertheless, the results at the lowest values of  $x$  ( $x < 0.1$ ) appear to be sensitive to the different regions of  $Q^2$  involved in the different analyses, and perhaps even to the analysis methods themselves. As a consequence, the precise shape of the distributions, which is largely determined by the data at low  $x$ , is somewhat uncertain. This should be kept in mind when comparing antiquark momentum distributions obtained from different neutrino experiments and from different processes, e.g.,  $p + p \rightarrow \mu^- + \mu^+ + X$ .

Comparison of the momentum distribution of

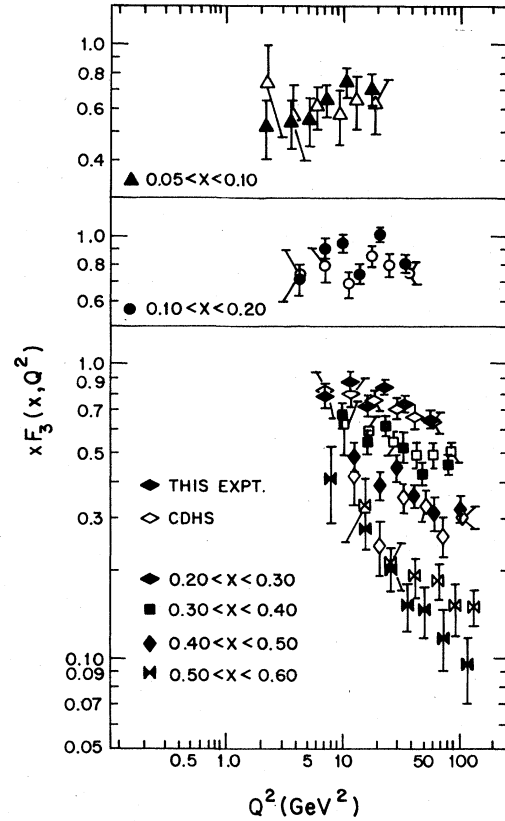


FIG. 40. A comparison of  $x F_3(x, Q^2)$  as a function of  $Q^2$  in several intervals of  $x$  from this experiment (solid symbols) and the CDHS experiment (open symbols, Ref. 12). Note the first interval for CDHS is  $0.06 < x < 0.10$ .

antiquarks, represented by  $x[\bar{u}(x) + \bar{d}(x) + \frac{3}{2}\bar{s}(x) + \frac{1}{2}\bar{c}(x)]$ , with the distribution for strange antiquarks alone  $x\bar{s}(x)$  in Fig. 36 shows the two distributions to be quite similar. Within the uncertainties of the two measurements, no indication of the different effective masses of ordinary and strange antiquarks is manifested.

Finally, the structure functions  $F_2$  and  $x F_3$  given as functions of  $x$  and  $Q^2$  in Figs. 37 and 38 show clearly the variation of the  $Q^2$  dependence in different regions of  $x$  that was observed earlier and is consistent with the weak dependence on  $Q^2$  predicted by QCD. Comparison of  $F_2(x, Q^2)$  and  $x F_3(x, Q^2)$  from this experiment with the results of another high-statistics neutrino experiment, shown in Figs. 39 and 40, is of special interest. The agreement between the experiments, particularly in the  $Q^2$  dependence, is excellent.

It is worth emphasizing that the data in Figs. 39 and 40 were obtained in two experiments that utilized very different experimental configurations and techniques. The general agreement of the data from the two experiments is, therefore, all

the more convincing. The regions of disagreement remain to be resolved by future more precise experiments which will require very large data samples to improve significantly on the results from the total data now accumulated.

## VI. ACKNOWLEDGMENTS

It is a pleasure to acknowledge the encouragement and support of this experiment provided by R. R. Wilson, E. L. Goldwasser, J. R. Sanford, and J. Peoples in their administrative capacities

at Fermilab. The Fermilab accelerator and computer staffs and the staffs of our university physics departments contributed with hard work and fine spirit to the success of the experiment. Special thanks are due Dixon Bogert and the staff of the Fermilab Film Analysis Facility for their excellent work. One of us (F.B.) thanks the Italian Istituto Nazionale Fisica Nucleare for financial support during the last part of the analysis. This work was supported in part by the U. S. Department of Energy and the U. S. National Science Foundation.

\*Now at Department of Physics, University of Pennsylvania, Philadelphia, Pennsylvania 19104.

†Now at CERN, Geneva, Switzerland.

‡Now at Department of Physics, Harvard University, Cambridge, Massachusetts 02138.

§Visitor at the University of Pennsylvania, now at Istituto di Fisica Dell'Università, Padova, Italy.

||Now at Department of Physics, Yale University, New Haven, Connecticut 06250.

¶Now at Laboratory for Nuclear Studies, Cornell University, Ithaca, New York 14853.

\*\*Now at Institute of Applied Physics, University of Tsukuba, Japan.

††Now at Saclay, Gif-sur-Yvette, France.

‡‡Now at Department of Physics, Louisiana State University, Baton Rouge, Louisiana 70803.

<sup>1</sup>R. P. Feynman, Phys. Rev. Lett. **23**, 1415 (1969); in *High Energy Collisions*, edited by C. N. Yang *et al.* (Gordon and Breach, New York, 1969); J. D. Bjorken and E. A. Paschos, Phys. Rev. **185**, 1975 (1969).

<sup>2</sup>J. D. Bjorken, Phys. Rev. **179**, 1547 (1969); J. D. Bjorken and E. A. Paschos, Phys. Rev. **D 1**, 3151 (1970).

<sup>3</sup>Two reviews that summarize the early development of QCD are: D. Gross and F. Wilczek, Phys. Rev. **D 8**, 3633 (1973) and H. D. Politzer, Phys. Rep. **14C**, 131 (1974). An excellent brief review of the QPM and lengthy review of recent developments in QCD is A. J. Buras, Rev. Mod. Phys. **52**, 199 (1980).

<sup>4</sup>A. Benvenuti *et al.*, Phys. Rev. Lett. **42**, 149 (1979); **42**, 1317 (1979). See, also, F. Bobisut, in *Neutrinos—78*, proceedings of the International Conference on Neutrino Physics and Astrophysics, edited by Earle C. Fowler (Purdue University Press, W. Lafayette, Indiana, 1978), and A. K. Mann, in *Current Hadron Interactions*, proceedings of the XIV Rencontre de Moriond, Les Arcs, France, 1979, edited by J. Trân Thanh Vân (Éditions Frontières, Dreux, France, 1979), p. 397.

<sup>5</sup>Results of the multimuon phase of the experiment can be found in the following papers: A. Benvenuti *et al.*, Phys. Rev. Lett. **38**, 1110 (1977); **38**, 1183 (1977); **40**, 488 (1978); **41**, 725 (1978); **41**, 1204 (1978); **42**, 149 (1979); **42**, 1024 (1979); S. Mori *et al.*, *ibid.* **40**, 432 (1978); David Winn, Ph.D. dissertation, University of Wisconsin, 1979 (unpublished) and James A. Rich, Ph.D. dissertation, Harvard University, 1979 (unpublished).

lished).

<sup>6</sup>(a) A. Benvenuti *et al.*, Nucl. Instrum. Methods **125**, 447 (1975); **125**, 457 (1975); (b) S. M. Heagy, Ph.D. dissertation, University of Wisconsin, 1980 (unpublished).

<sup>7</sup>J. Sanford, Ann. Rev. Nucl. Sci. **26**, 151 (1970).

<sup>8</sup>A. Skuja *et al.*, Fermilab Technical Memo No. TM626a, 1970 (unpublished).

<sup>9</sup>R. J. Stefanski and H. B. White, Fermilab Technical Memo No. TM646, 1976 (unpublished).

<sup>10</sup>D. Bogert *et al.*, in Proceedings of the Oxford Conference on Computer Scanning, 1974 (unpublished).

<sup>11</sup>A. De Rújula, R. Petronzio, and A. Savoy-Navarro, Nucl. Phys. **B154**, 391 (1979).

<sup>12</sup>References here are from a revised version of a figure in a paper by D. Theriot, in *Proceedings of the 1979 International Symposium on Lepton and Photon Interactions at High Energies, Fermilab*, edited by T. B. W. Kirk and H. D. I. Abarbanel (Fermilab, Batavia, Illinois, 1979), p. 337. (1) Caltech-Fermilab-Rochester-Rockefeller (CFRR): B. Barish *et al.*, Caltech Report No. CALT 68-734, 1979 (unpublished); (2) Caltech-Fermilab-Rockefeller (CITFR): B. C. Barish *et al.*, Phys. Rev. Lett. **39**, 1595 (1977); (3) CERN-Dortmund-Heidelberg-Saclay (CDHS): J. G. H. de Groot *et al.*, Z. Phys. **C 1**, 143 (1979); (4) Gargamelle (GGM): S. Ciampolillo *et al.*, Phys. Lett. **84B**, 281 (1979); (5) Big European Bubble Chamber (BEBC): D. C. Colley *et al.*, Z. Phys. **C 2**, 187 (1978); (6) ANL: S. J. Barish *et al.*, Phys. Rev. **D 19**, 2521 (1979); (7) IHEP-ITEP: A. E. Asratyan *et al.*, Phys. Lett. **76B**, 239 (1978), and A. E. Mukhin, Serpukov Report No. SERP-E-45, 1979 (unpublished).

<sup>13</sup>GGM: T. Eichten *et al.*, Phys. Lett. **46B**, 274 (1973); Harvard-Pennsylvania-Wisconsin-Fermilab (HPWF-1A1): A. Benvenuti *et al.*, Phys. Rev. Lett. **36**, 1478 (1976); Caltech-Fermilab (CTF): F. Sciulli, in *Proceedings of the International Symposium on Lepton and Photon Interactions at High Energy, Hamburg, 1977*, edited by F. Gutbrod (DESY, Hamburg, Germany, 1977): B. C. Barish *et al.*, Phys. Rev. Lett. **40**, 1414 (1978); Fermilab-ITEP-Michigan-Serpukhov (FIMS): Fermilab-IHEP-ITEP-Michigan Neutrino Group, Phys. Rev. Lett. **39**, 382 (1977); BEBC: P. C. Bosetti *et al.*, Phys. Lett. **B70**, 273 (1977).

<sup>14</sup>B. C. Barish *et al.*, Phys. Rev. Lett. **38**, 314 (1977); **40**, 1414 (1978); J. G. H. de Groot, Ref. 12.

<sup>15</sup>T. Trinko *et al.* (unpublished).



- <sup>16</sup>Parametrizations suggested, for example, by V. Barger and R. J. N. Phillips, Nucl. Phys. **B73**, 269 (1974); A. J. Buras and K. J. F. Gaemers, *ibid.* **B132**, 249 (1979) and references therein.
- <sup>17</sup>ANL: S. J. Barish *et al.*, Ref. 12; SKAT: D. S. Baranov *et al.*, Phys. Lett. **76B**, 366 (1978); CDHS: K. Tittel, in *Proceedings of the 19th International Conference on High Energy Physics, Tokyo, 1978*, edited by S. Homma, M. Kawaguchi, and H. Miyazawa (Physical Society of Japan, Tokyo, 1979), p. 863; GGM: T. Eichten *et al.*, Ref. 13; BEBC: P. C. Bosetti *et al.*, Ref. 13; Fermilab: J. P. Berge *et al.*, Phys. Rev. Lett. **36**, 639 (1976); IHEP-ITEP: A. E. Asratyan *et al.*, Ref. 12.
- <sup>18</sup>P. C. Bosetti *et al.*, Nucl. Phys. **B142**, 1 (1978); M. D. Mestayer, Report No. SLAC-PUB-214, 1978 (unpublished); D. Buchholz, in *Proceedings of the 19th International Conference on High Energy Physics, Tokyo, 1978*, edited by S. Homma, M. Kawaguchi, and H. Miyazawa (Physical Society of Japan, Tokyo, 1979), p. 328; J. G. H. de Groot, Ref. 12.
- <sup>19</sup>Y. Wanatabe *et al.*, Phys. Rev. Lett. **35**, 898, 901 (1975); E. M. Riordan *et al.*, Report No. SLAC-PUB-1634, 1975 (unpublished); J. C. Taylor, in *Proceedings of the 1975 International Symposium on Lepton and Photon Interactions at High Energies, Stanford*, edited by W. T. Kirk (SLAC, Stanford, 1976); W. B. Atwood *et al.*, Phys. Lett. **64B**, 479 (1976); B. A. Gordon *et al.*, Phys. Rev. Lett. **41**, 615 (1978); A. Bodek *et al.*, Phys. Rev. D **20**, 1471 (1979); H. L. Anderson *et al.*, in *Proceedings of the 19th International Conference on High Energy Physics, Tokyo, 1978*, edited by S. Homma, M. Kawaguchi, and H. Miyazawa (Physical Society of Japan, Tokyo, 1979); see also Phys. Rev. Lett. **37**, 4 (1976); **38**, 1450 (1977).